Title: Extracellular matrix remodeling during aging aligns with synapse, microglia, and cognitive status

Authors: Daniel T. Gray[1], Abigail Gutierrez[1], Yasaman Jami- Alahmadi [2], Vijaya Pandey[2], Lin Pan[3], Ye Zhang[3], James A. Wohlschlegel[2], Ross A. McDevitt[4], Lindsay M. De Biase[1]

Author Affiliations:

1. Department of Physiology, David Geffen School of Medicine, University of California, Los Angeles. Los Angeles, CA 90095
2. Department of Biological Chemistry, David Geffen School of Medicine, University of California, Los Angeles. Los Angeles, CA 90095
3. Department of Psychiatry and Biobehavioral Sciences, Semel Institute for Neuroscience and Human Behavior, David Geffen School of Medicine, University of California, Los Angeles. Los Angeles, CA 90095
4. Comparative Medicine Section, National Institute on Aging Intramural Research Program, Baltimore, MD 21224, United States of America

Corresponding Author: Lindsay De Biase

Department of Physiology, David Geffen School of Medicine

University of California, Los Angeles

10833 Le Conte Avenue, 76-100E CHS; Los Angeles, CA 90095

E-mail address: lmdebiase@mednet.ucla.edu

Conflict of interest statement: The authors do not claim any conflicts of interest.

Abstract

Synapse dysfunction is tightly linked to cognitive changes during aging, but underlying mechanisms driving dysfunction are minimally understood. The extracellular matrix (ECM) can potently regulate synapse integrity and plasticity. Yet the status of the brain ECM during aging remains virtually unexplored. Using novel ECM-optimized proteomic workflows, we discovered striking regional differences in ECM composition and aging-induced ECM remodeling. ECM status was also aligned with preserved synapse protein abundance across key basal ganglia nuclei. Moreover, using foraging-based behavioral paradigms and confocal imaging in fixed tissue, we demonstrated that reduced ECM-synapse remodeling and microglial aging phenotypes are both linked with deficits in goal-directed behavior in aging mice. Finally, using mouse models of microglia ablation and premature microglial aging, we identified microglial aging phenotypes that promote ECM deposition and synapse numbers. Together, these foundational observations implicate glial-ECM interactions in the regulation of synapse function and cognitive abilities across the lifespan.

Main

Synapse loss and changes in synaptic plasticity are hallmark features of both normative brain aging and preclinical phases of neurodegenerative disease [1–3]. These synaptic changes have critical consequences, as preserved synapse status is linked to better cognitive outcomes in healthy aged rodents and nonhuman primates [1,4]. Growing evidence suggests the extracellular matrix (ECM) is a robust regulator of synaptic physiology during development and in early adulthood[5,6]. The ECM is not a static structure, but rather a dynamic network of proteins and carbohydrates remodeled to support numerous brain functions including synaptic plasticity and tissue repair [5–7]. Histochemical staining of ECM components suggests that ECM abundance[8] and composition[9,10] vary across brain regions and ECM remodeling can occur during aging [7,11,12]. This raises the possibility that ECM status may determine vulnerability of specific brain regions to aging-related synaptic decline.

Microglia, the primary brain immune cells, also regulate synapses[13–18], including through a recently discovered mechanism involving targeted degradation of ECM proteoglycans[7,19,20]. Microglia are sensitive to numerous perturbations of the CNS microenvironment and their properties are substantially altered during aging. Moreover, changes in microglial density are associated with ECM alterations in mouse models of Alzheimer's Disease and aging macaques [21 22]. Together, these observations suggest that changes in microglial regulation of the ECM may play central roles in shaping synapse dynamics during aging, patterns of age-associated cognitive decline, and neurodegenerative disease susceptibility. Yet, this microglia-ECM-synapse triad remains virtually unexamined in most brain regions in both young adulthood and aging.

Microglia exhibit stark regional specializations that likely influence their interactions with the ECM [23,24]. These regional differences are especially prominent across nuclei of the basal ganglia dopamine system [23], and microglia near dopamine neurons exhibit increases in

proliferation and inflammatory factor production earlier in the lifespan compared to microglia in other basal ganglia nuclei[25]. Moreover, numerous cognitive deficits associated with normative aging have been linked with dysregulation in dopaminergic systems [26,27]. Together, these characteristics make mesolimbic dopamine circuits ideal for mapping how regional specializations in microglial-ECM-synapse responses to aging align with individual differences in cognition. The present study combines high-resolution imaging, quantitative tissue proteomics, goal-directed behaviors, and genetic inductions of microglial depletion and accelerated aging to link microglia, synapse, and ECM status across the mesolimbic dopamine system with cognitive aging outcomes.

Results

Novel ECM-optimized proteomics reveals strong association between ECM and synapse status in the aging basal ganglia

ECM proteins are highly glycosylated and comparatively insoluble, making it difficult to leverage traditional proteomic approaches to comprehensively map the brain ECM (i.e., matrisome). We compared two pre-proteomics ECM-enrichment strategies that have been used for analysis of ECM in peripheral tissues throughout the body, solubility-based tissue fractionation[28] and chaotropic extraction and digestion[29]. This analysis revealed that solubility-based fractionation identified slightly more structural ECM proteins (core matrisome) in brain tissue (**Figure 1a, Ext. Data Fig. 1**). Using this solubility-based workflow, we then created the first comprehensive proteomic mapping of the aging ECM proteome in two key basal ganglia nuclei from wildtype mice.

In general, matrisome proteins in the most insoluble fractions were more abundant in aged (20+ months) mice compared to young (3 months) mice and found at higher levels in the midbrain compared to striatum (**Figure 1b, Ext. Data Fig. 2**). Volcano plots of protein abundance show that most core matrisome proteins increase during aging, whereas overall tissue proteins, analyzed by interrogating all solubility fractions, are more evenly split between up- and down-regulated proteins (**Figure 1c**).

Core matrisome proteins fall into 3 subclasses: collagens, glycoproteins, and proteoglycans. Collagen abundances varied prominently across brain region, with eight distinct collagens detected in the midbrain compared to just two in striatum (**Figure 1d**). Moreover, several midbrain collagens showed significant increases in abundance during aging. Comparable numbers of ECM glycoproteins were detected in the midbrain and striatum, and several were significantly upregulated in both regions with aging (Tenascin C, VWA 1, TARP).

However, Laminin glycoproteins showed prominent regional differences and were specifically upregulated in the aging striatum (**Figure 1e**). Finally, more proteoglycans were detected in midbrain compared to striatum and were generally more abundant in the midbrain. Nearly 50% of midbrain proteoglycans showed significant increases in abundance with age compared to just 1 in the striatum (**Figure 1f**). Together, these observations demonstrate that regional heterogeneity in ECM composition and modulation during aging extends to all three subclasses of ECM proteins.

To relate matrisome status with other features of the whole tissue proteome, Weighted Gene Coexpression Network Analysis[30] was leveraged for unbiased identification of protein co-expression patterns (**Figure 2a**). This analysis identified 12 modules of covarying proteins. Most core matrisome proteins (~82%) were members of yellow, brown, or tan modules (**Figure 2a**) highlighting these as warranting further analysis. Innate immune proteins, which can play key roles in synapse remodeling[17], were also found within yellow (15%) and brown modules (12%), in addition to prominent presence in the turquoise (33%) module. Examination of module eigengenes revealed stark regional differences between the midbrain and striatum for the brown, yellow, and tan modules, but not the turquoise module (**Figure 2b**). Pathway analysis indicated that brown module proteins were associated with numerous metabolic processes, yellow with chemical synaptic transmission and structure, turquoise with RNA metabolism and translation, and tan with a mix of biological processes including ECM organization (**Figure 2c**).

To further evaluate relationships between these modules and ECM, synapse, and immune proteins, we treated individual ECM, synapse, and immune protein abundances as “traits” and determined whether these were correlated with module eigengenes across samples (**Figure 2d**). Striking associations were observed between ECM proteoglycans and brown/yellow/tan module eigengenes, with HAPLN1-4 and aggrecan showing significant correlations. While many immune signaling proteins also showed significant associations with

brown/yellow/tan module eigengenes (**Ext. Data Fig. 3**), complement proteins C1qA and C1qB, which are known to tag synapses for microglial engulfment[17], were only significantly correlated with turquoise module eigengenes. Finally, numerous synaptic proteins showed relationships with brown/yellow/tan module eigengenes, whereas very few did with the turquoise module. Collectively, these observations suggest that synaptic and ECM protein abundances are tightly linked in the basal ganglia, and that complement signaling is not related to ECM deposition.

Abundance of most synaptic proteins did not differ between young-adult and aged mice, indicating that substantial synapse *loss* is not occurring in the midbrain and striatum during healthy aging (**Ext. Data Fig. 4**). This aligns with previous reports showing that while synapse loss does occur in certain vulnerable brain regions during healthy aging, synapse numbers remain relatively constant in many others[1,31]. To further explore relationships between age-associated changes in ECM composition (**Figure 1**) and basal ganglia synapse status, we carried out additional pathway analysis focusing on module proteins significantly altered during aging. Plotting identified pathways as network plots, revealed interconnected clusters of brown/yellow/tan module proteins associated with ECM organization and ECM-receptor interactions in the midbrain. This cluster was directly connected to clusters associated with synapse organization (**Figure 2e**), meaning that functional annotation predicts that proteins within these pathway “nodes” influence one another. While similar ECM clusters were also observed in the striatum, they were not directly connected to any pathway nodes associated with synapse organization. These observations argue that age-associated ECM remodeling has a distinct relationship with local synapse status across different regions of the aging brain.

A group of turquoise module proteins associated with antibody-mediated complement system activation was also observed specifically in the midbrain (**Figure 2e**). However, this cluster of pathways was not connected to pathway nodes involved in synaptic function, nor to other identified turquoise module pathway clusters. These finding are somewhat unexpected

given that complement system activation has been observed in several pathological aging contexts[32–34]. Moreover, they suggest that ECM composition plays a more central role than complement-mediated synapse regulation in determining basal ganglia synapse status during healthy aging. This may represent a crucial difference between normative and pathological aging trajectories in these regions.

Together, this first-of-its-kind proteomic mapping of matrisome, synapse, and immune proteins indicates that, in a normative aging context, regional variation in ECM status plays key roles in establishing and/or maintaining regional basal ganglia synapse profiles.

Hyaluronan networks differ across region and age and show spatial interactions with excitatory postsynaptic elements in mesolimbic dopamine circuits

Although proteomic approaches provide unbiased and comprehensive quantification of ECM composition in targeted brain regions, they cannot reveal the morphology and spatial distribution of ECM components. For independent analysis of the brain ECM during aging, we histologically examined the glycosaminoglycan hyaluronan, a ubiquitous ECM scaffold to which proteoglycans and other glycosylated proteins are attached. In this capacity, hyaluronan scaffolds play central roles in determining overall ECM tissue topology [20,35]. High-resolution (63x) confocal images of histochemically labeled hyaluronan were acquired from young-adult (4 months) and late-middle-aged (18 months), wild-type, C57Bl6 mice within the ventral tegmental area (VTA, midbrain), where microglia were previously shown to exhibit early responses to aging [25], and nucleus accumbens (NAc, ventral striatum), where early microglial aging was not observed.

Hyaluronan fibril density, size, and distribution regularity were greater in the VTA compared to NAc (**Figure 3a-3e**). Hyaluronan fibril density and distribution regularity were also

higher in the VTA during aging, but not NAc (**Figure 3c-3e**). Analysis of hyaluronan properties during aging in numerous other brain regions, including several extending beyond the basal ganglia, suggests the hyaluronan matrix accumulations are a particularly prominent feature of VTA aging (**Ext. Data Fig. 5**). Together these findings are consistent with proteomic detection of greater midbrain hyaluronan link protein levels during aging (**Figure 1f**) and indicate that hyaluronan matrix structure undergoes age-dependent modifications in certain regions where microglia exhibit early responses to aging.

Proteoglycans anchored to hyaluronan can impact synapses via multiple mechanisms, including limiting structural remodeling and regulating lateral diffusion of neurotransmitter receptors[7,36]. To relate hyaluronan structure to local synapse status, densities of homer2, a postsynaptic excitatory synapse protein, were quantified in the VTA and NAc (**Figure 3f**). Homer2 densities were greater in the NAc compared to VTA but not different between young-adult and late-middle-aged mice in either region (**Figure 3g**), consistent with proteomic data suggesting minimal synapse loss in the aging midbrain and striatum. To probe spatial relationships between hyaluronan and homer2, hyaluronan fibrils were tagged and dilated by 0.5 μm, to estimate the density of homer2 puncta within the potential territory of proteoglycans anchored to this scaffold (**Figure 3h**)**.** In both VTA and NAc, hyaluronan-homer2 spatial associations were greater than would be expected by chance (associations detected when one fluorescence channel was rotated 90 degrees, **Figure 3i**), supporting the idea of functional associations between local ECM and synapses. The density and proportion of homer2 within 0.5 μm of hyaluronan was similar in young-adult and late-middle-aged mice and not different across regions, although greater variability was observed in the NAc. Together, these histological findings validate regional ECM heterogeneity revealed by proteomics, confirm regional differences in the impact of age on the local ECM, and suggest that ECM-synapse spatial associations occur throughout life.

VTA hyaluronan and synapse network remodeling aligns with reward-based memory impairment in middle-aged mice

Midbrain dopaminergic signals enhance learning and memory processes by modulating synaptic plasticity across the forebrain, signaling reward, salience, and novelty[37]. Altered dopamine system function has been implicated in numerous cognitive deficits associated with normative aging, including reductions in cognitive flexibility, attentional control, and working memory[26]; yet whether aging-induced changes in the ECM contribute to this dysfunction remains unexplored. To test this, we developed a behavioral paradigm that engages reward circuitry and probes aspects of reward-based cognition. (**Figure 4a, 4b**). In this paradigm mice learn to explore a large arena and forage for palatable food reward that changes location daily. During testing (probe trials), mice encode a rewarded location and after 2 or 24 hours reenter the arena with 4 unrewarded feeders to measure their memory of the rewarded location. In total, mice undergo 5 weeks of training/testing (5 days/week), which allows for robust assessment of cognitive status of individual mice and minimizes behavioral variables like novelty and stress by the point at which brain tissue is collected for histological examination.

Both young-adult (4 months) and late-middle-aged (18 months) non-food-restricted mice learned the task and exhibited consistent foraging at similar points in the experiment timeline (**Figure 4c-4d, Ext. Data Fig. 6**). Interestingly, during training when reward is present during retrieval, the middle-aged mice performed better than young (**Figure 4e**). Average walking speeds, exit latencies, and proportion of time on the arena's perimeter did not differ between age groups, indicating similar levels of task engagement and absence of prominent anxiety-like behavior (**Figure 4f-4h).** During probe sessions, young-adult mice performed similarly and better than chance following both 2- and 24-hour delays. Middle-aged mice performed comparably to young-adult mice with a 2-hour delay but made fewer correct feeder visits and

more errors following 24-hour delays (**Figure 4i, 4j**). Critically, we observed significantly higher variability in middle-aged mice during 24-hour probe trials compared to young, which is a hallmark of cognitive aging[38]. Hence, this nuanced behavioral paradigm establishes a strategy to probe links between neurobiological factors in mesolimbic dopaminergic circuits and normative age-associated changes in reward-based cognition.

Because behavioral training/testing occurs over 5 weeks, as an additional control, each cohort of mice included sedentary controls to enable detection of any cellular and molecular changes induced by behavior training (**Figure 5a**). Compared to sedentary mice, behavior-trained mice exhibited significantly less hyaluronan within the VTA (**Figure 5b, 5c, Ext. Data Fig. 7**), particularly in middle-aged mice. Hence, the accumulation of VTA hyaluronan observed in aging sedentary animals was no longer apparent in aging behavior-trained mice. Furthermore, middle-aged mice with lower hyaluronan densities exhibited better task performance (**Figure 5d**), indicating that this ECM remodeling is beneficial. Behavior-induced hyaluronan network remodeling was not observed in multiple other brain regions examined, including the substantia nigra pars compacta, NAc, hippocampus, and cortex (**Ext. Data Fig. 7**), suggesting that ECM remodeling occurs specifically around mesolimbic dopamine neurons when animals repeatedly engage with reward-based tasks.

To link behavior-induced VTA hyaluronan matrix remodeling with synapse status, homer2 was also analyzed in these mice. Compared to sedentary mice, behavior-trained mice had elevated homer2 puncta densities, indicating that behavioral training/testing had net synaptogenic effects (**Figure 5e, 5f**). However, surprisingly, mice with fewer synapses showed better task performance (**Figure 5g**), suggesting that performance-enhancing synapse refinement may also occur across this 5-week paradigm. Moreover, hyaluronan and homer2 densities within individual fields of view were not correlated in sedentary mice. After behavioral training, however, robust positive correlations between hyaluronan and homer2 densities

emerged (**Ext. Data Fig. 8**), indicating that behavior-associated remodeling of hyaluronan and homer2 are likely intertwined. We also examined synapses specifically on dopamine neurons (TH-homer2; **Figure 5h**) and found that middle-aged animals with less TH-homer2 exhibited better task performance (**Figure 5i, 5j**), suggesting that observed field of view changes in VTA hyaluronan and synapse density in response to behavioral training are likely to impact activity and function of dopamine neurons. Indeed, hyaluronan deposition on dopamine neurons was strongly positively correlated with the number of synapses on dopamine neurons in behavior-trained mice, but not sedentary controls, (**Figure 5k**). Taken together, these experiments suggest that greater abundance of VTA hyaluronan matrix promotes excitatory synapse numbers, but may limit synaptic refinements that optimize circuit function for reward-driven behavior.

Microglia aging phenotypes correlate with reward-based memory

Microglia exhibit prominent regional heterogeneity in cellular phenotype, and VTA microglia exhibit premature responses to aging compared to microglia in the NAc[23,25]. However, whether microglia aging phenotypes around dopamine neurons represent vulnerabilities or adaptive changes that preserve circuit function is unknown. To begin answering this question, IBA1-positive VTA and NAc microglia densities were examined with respect to task performance. As shown previously, microglia densities were higher in the NAc compared to VTA and increased with age only in the VTA (**Figure 6a, 6b**). Mice with more VTA microglia exhibited worse task performance, and this relationship was significant even when examining only middle-aged mice (**Figure 6c, Ext. Data Fig. 8**). Surprisingly, NAc microglia densities showed the opposite relationship, where mice with greater microglial densities exhibited better performance. These findings indicate that regional microglial specializations and aging phenotypes uniquely impact the neuronal circuits in which they reside.

To further explore how VTA microglial status relates to reward-based behavior, we acquired 63x confocal images of IBA1-positive microglia and hyaluronan. While VTA microglia tissue coverage was similar in behavior-trained and sedentary mice, mice with greater microglial coverage exhibited poorer task performance (**Figure 6d-6f**). Regardless of behavioral training, middle-aged mice with greater microglial tissue coverage exhibited more VTA hyaluronan (**Figure 6g, 6h**). Since middle-aged mice with greater VTA hyaluronan showed worse reward-based memory (**Figure 5d**), this finding indicates that aging VTA microglia may negatively impact behavior by promoting excess ECM deposition and limiting synapse remodeling.

VTA microglia structure is aligned with local hyaluronan networks

Microglia express receptors that could enable direct "sensing" of nearby matrix, degradative enzymes that can alter ECM structure, and synthetic enzymes that could contribute to production of ECM components [7,20,39]. Yet, almost nothing is known about microglial-ECM interactions during aging. To further explore how microglial status relates to local ECM structure across the lifespan, we analyzed tissue from young (3-4 months), middle-aged (12-17 months), and aged (18-22 months) *Cx3Cr1*$^{EGFP/+}$ mice, which enables precise visualization of microglial morphology (**Figure 7a**). In the VTA, greater microglial tissue coverage was significantly correlated with greater hyaluronan matrix deposition in young and aged mice (**Figure 7b**), consistent with findings in wildtype mice (**Figure 6g**). In contrast, NAc microglial tissue coverage was not related to hyaluronan distribution at any age. More localized analysis of hyaluronan-microglial relationships was carried out by overlaying a 10x10 grid on each confocal image, quantifying hyaluronan and GFP abundance within each grid square, and performing regression analyses for each image (**Figure 7c**). Significant relationships between hyaluronan and microglia tissue coverage were observed in 78% of VTA images and 73% of NAc images. Correlation coefficients were consistent across ages in the VTA (r = 0.4-0.75) but increased with

age in the NAc (young: r = -0.1-0.3; middle-aged/aged: r = 0.25-0.78; **Figure 7d**). These data suggest that there is prominent regional heterogeneity in the extent to which microglia can impact hyaluronan distribution within their immediate vicinity, or vice versa. In the NAc, where microglia exhibit only modest aging phenotypes[25], microglia coverage is only related to the local distribution of hyaluronan later in the lifespan. In the VTA, however, where microglial exhibit prominent aging phenotypes by early-middle age[25], microglia coverage is related to both local hyaluronan matrix deposition, and hyaluronan distribution across other parts of the parenchyma. These finding further suggest that VTA microglia aging phenotypes somehow promote changes in ECM composition around VTA dopamine neurons, or that aging-associated changes in ECM composition within the VTA promote the emergence of microglia aging phenotypes.

Microglia attenuate ECM deposition in the young-adult VTA

To probe the observed correlation between greater hyaluronan deposition and greater microglial tissue coverage in the VTA, we examined tissue from young adult (3-4 months) microglia-deficient mice ($Csf1r^{\Delta FIRE/\Delta FIRE}$ mice; **Figure 8a**)[40]. Compared to control mice, $Csf1r^{\Delta FIRE/\Delta FIRE}$ mice exhibited higher VTA hyaluronan densities but no difference in homer2 puncta densities (**Figure 8b, 8c**), similar to observations in aging wild-type mice (**Figure 3**). Together with findings that the VTA hyaluronan matrix accumulates with age (**Figure 3**), these observations suggest that young-adult microglia attenuate ECM deposition in the VTA and that this microglial function is diminished with normative aging. While elevated hyaluronan deposition was not associated with altered numbers of postsynaptic structures in either aging wildtype or microglia-deficient mice, these changes likely impact proteoglycan deposition around synapses and modify capacity for synapse plasticity[5].

Microglial Cx3Cr1 deficiency alters VTA microglia-ECM-synapse interactions during aging

CX3CR1 deficiency has been suggested to accelerate microglial aging phenotypes [25,41], impact synaptic plasticity [42], and regulate ECM composition in other bodily tissues [43,44]. To further probe how microglial aging trajectories impact the ECM and synapses, hyaluronan and homer2 were analyzed in young-adult (3-4 months) and early-middle-aged (12-15 months) Cx3Cr1-het (*Cx3Cr1*$^{EGFP/+}$) and Cx3Cr1-KO (*Cx3Cr1*$^{EGFP/EGFP}$) mice (**Figure 8d**).

VTA microglia from Cx3Cr1-KO mice exhibited reduced morphological complexity compared to Cx3Cr1-het mice, particularly at middle-age, confirming that this manipulation enhances key microglial aging profiles (**Ext. Data Fig. 9**). VTA hyaluronan fibril densities were similar in middle-aged Cx3Cr1-het mice compared to young but were significantly lower in middle-aged Cx3Cr1-KO mice compared to young (**Figure 8e**), which is opposite of what was observed in aging wildtype mice. Both Cx3Cr1-het and Cx3Cr1-KO mice exhibited significant reductions in homer2 density by middle age, suggesting that, unlike wildtype mice (**Figure 3g**), Cx3Cr1-deficient mice exhibit age-associated VTA synapse loss (**Figure 8f**). Analysis of colocalization between microglia, hyaluronan, and homer2 indicated that putative microglial hyaluronan engulfment was not significantly different in either genotype, although aging Cx3Cr1-KO microglia tended to contain more hyaluronan (**Figure 8g, 8h**). Putative microglial synapse engulfment was lower at middle-age in both genotypes (**Figure 8i**), indicating that age-associated reductions in synapse density in these mice do not arise from greater microglial synapse engulfment. Together these results suggest that, during normative aging, Cx3CR1 signaling promotes microglial states permissive of ECM accumulation, and that loss of Cx3CR1 signaling reduces both ECM abundance and excitatory synapse numbers in the aging VTA, potentially via enhanced microglial engulfment of the ECM.

Discussion

As the predominant structure occupying the extracellular space, the ECM is positioned to play central roles in almost all neurological processes. Yet, brain ECM research is still nascent, and optimal strategies for observing and measuring the ECM's complexity are still being defined. Revealing how the ECM impacts discrete brain structures – such as synapses – is a challenge for the field. ECM-synapse contact can regulate AMPA receptor diffusion and positioning of neuronal pentraxins [32,47]. ECM abundance near synapses can also impact extracellular ion concentrations and regulate access of phagocytic cells to synaptic elements [20,46]. Moreover, the "sweet spot" of optimal ECM abundance near synapses depends on context; appropriate ECM deposition may protect against synapse loss, but targeted degradation of ECM components is also essential for structural plasticity in support of learning and memory [7]. Advancing knowledge in this area is likely to promote a paradigm shift in how we view regulation of synaptic function and such work promises to illuminate novel approaches to manipulate the brain ECM in support of healthy circuit function.

This report presents the first comprehensive proteomic mapping of the brain ECM during aging and reveals stark regional heterogeneity in ECM composition and age-associated ECM remodeling across the basal ganglia. This finding argues that similar mapping of additional brain regions in a wide variety of contexts (CNS development, brain injury, brain cancer, neurodegeneration, to name a few) is urgently needed in the field. In general, we found that basal ganglia matrisome proteins increased during aging, and histological examination of the core ECM scaffold hyaluronan confirmed this increase, aligning with previous biochemical and gene expression studies showing increased hyaluronan production in normative aging contexts[42,43]. Our proteomic and histological examination also revealed that robust synapse loss was not a feature of healthy midbrain or striatal aging, at least at the ages we examined. Nonetheless, unbiased computational analyses of our proteomic data revealed that overall

abundance and composition of synaptic proteins was strongly aligned with abundance and composition of ECM proteins, arguing that even in the absence of changes in synapse number, there is a critical role for the ECM in shaping synapse function. In terms of regional differences in ECM-synapse relationships, we found that the NAc has significantly more excitatory postsynaptic structures and less hyaluronan matrix deposition compared to the VTA. This may imply that NAc networks are more malleable as the ECM is thought to restrict plasticity since, for example, the closing of developmental critical periods aligns with drastic increases in ECM abundance [48]. Furthermore, it may suggest that although excitatory VTA synapse numbers remain stable with age, VTA synapses in older animals may be more rigid as ECM deposition increases.

Surprisingly, our unbiased computational analysis of proteomic data also revealed that status of synaptic proteins was not aligned with complement system proteins. Microglial synapse engulfment through complement tagging has been implicated in numerous disease contexts [17,44,45]. Our observation of steady synapse numbers and lack of association between synaptic proteins and complement proteins, suggests that local ECM status plays more prominent roles than complement deposition in determining synapse status in the context of healthy brain aging.

Numerous cognitive deficits associated with normative aging are believed to involve dysfunction in mesolimbic dopamine circuits [26,27]. A critical and powerful element of our study design was inclusion of a reward-based behavioral paradigm that enabled us to link cellular- and molecular-level observations about the ECM and synapses to cognitive status of individual young and aging mice. We found that reward-based behavioral training resulted in ECM remodeling around dopamine neurons characterized by less ECM deposition. Critically, middle-aged mice with greater ECM deposition within the VTA exhibited more excitatory postsynaptic puncta, but worse reward-based memory function. These findings indicate that preservation of

excitatory synapses onto dopamine neurons does not automatically translate into preserved cognition. Instead, age-related ECM accumulations in the VTA may constrain synapse remodeling necessary for optimal VTA circuit function.

One unique feature of the VTA is that microglia within this region exhibit accelerated aging phenotypes, characterized by increases in proliferation and inflammatory factor production, compared to microglia in other basal ganglia nuclei [25]. Here we provide the first links between VTA microglial aging phenotypes, age-related ECM accumulation patterns, and cognition. While microglial properties did not change as a result of behavioral training, aging mice with more microglia showed less behavior-induced ECM remodeling and worse reward-based memory. This indicates that VTA microglial aging phenotypes critically inform reward-based cognition during aging. Moreover, they demonstrate that microglial phenotypes that promote excess VTA ECM deposition likely limit the degree of synapse remodeling achievable within this circuit.

Several additional findings from our study further indicate that VTA microglial aging likely results in loss of capacity to remodel the ECM. First, constitutive microglial depletion phenocopies normative age-associated increases in hyaluronan matrix deposition, arguing that microglia typically restrict ECM deposition and that this ability is lost during aging. Furthermore, perturbing microglial aging trajectories via deletion of Cx3Cr1 results in decreased hyaluronan deposition and reduced excitatory postsynaptic puncta by early middle age. This differs from aging trajectories observed in wild-type mice, which exhibit greater hyaluronan deposition and stable synapse numbers. Neuron-microglia communication via CX3CL1/CX3CR1 signaling has been linked to various aspects of synapse regulation [39,49] and the present findings extend these observations by suggesting that complete loss of Cx3Cr1 signaling shifts microglia into hyper-phagocytic and/or hyper-degradative phenotypes that reduce ECM abundance, leading to synapse loss. An important future direction is to causally test how microglia modify ECM-

synapse interactions in behavior-trained genetic mouse models with manipulations to key microglial ECM-sensing proteins and ECM-degradative enzymes.

Finally, while VTA microglial aging phenotypes were negatively correlated with behavior, aging mice with more NAc microglia showed more precise goal-directed behavior. Hence, while some aspects of microglial aging represent vulnerabilities to circuit function, others may arise as adaptive responses that maintain neuronal network activity. As novel technologies emerge that allow for *in vivo* monitoring of specific ECM components, microglia-ECM interactions, and ECM-synapse interactions, such a framework (recognizing both detrimental and adaptive/beneficial aging-induced changes in microglia, ECM, and synapses) will be critical in linking regional specializations in microglia-ECM-synapse dynamics with synapse dysfunction and cognitive aging outcomes.

Material and Methods

Mice

This study uses C57Bl6 wild-type mice, CX3CR1$^{EGFP/+}$ and CX3CR1$^{EGFP/EGFP}$ mice, and Csf1r$^{+/+}$ and Csf1r$^{\Delta FIRE/\Delta FIRE}$ mice [40]. C57Bl6 wild-type mice used for behavioral and histochemical experiments were purchased from the National Institutes on Aging (NIA) colony (Bethesda, Maryland), and the mice used for proteomic mapping were purchased from Jackson Laboratory (Bar Harbor, ME; stock #000664). CX3CR1$^{EGFP/EGFP}$ breeders on a C57Bl6 background were originally purchased from the Jackson Laboratory (stock #005582) and crossed with C57Bl6 wild-type mice to obtain heterozygous (CX3CR1$^{EGFP/+}$) mice and CX3CR1$^{EGFP/EGFP}$ mice to obtain homozygous mice (CX3CR1$^{EGFP/EGFP}$). In these mice, EGFP is knocked into the fractalkine receptor (CX3CR1) locus, which is a receptor expressed specifically by most myeloid-lineage cells, including microglia [51]. Previous work has demonstrated that EGFP expression in these mice is specific to microglial cells in the basal ganglia [23]. Csf1r$^{\Delta FIRE/\Delta FIRE}$ breeders on a B6CBAF1/J background were originally purchased from Jackson Laboratory (stock # 032783) and crossed with C57BL/6 mice after which their offspring were interbred. These mice carry CRISPR/Cas9-generated deletion of the fms-intronic regulatory element (FIRE) of the Csf1r gene [40].

For immunohistochemical and histochemical experiments in sedentary wild-type mice, up to 12 young-adult (4 months; 6 male, 6 female) and 12 late-middle aged mice (18 months; 6 male, 6 female) were used. Analysis of microglia-ECM spatial relationships was performed on images obtained from 5 young-adult (3-4 months; 3 female, 2 male), 5 middle-aged (13-18 months, 3 female, 2 male), and 6 aged (21-24 months, 4 female, 2 male) CX3CR1$^{EGFP/+}$ mice. Histochemical quantifications of synapse and hyaluronan abundance in Cx3Cr1-deficient and knockout mice utilized 4 young-adult Cx3Cr1$^{EGFP/+}$ (3-4 months; 2 male, 2 female), 4 young-adult Cx3Cr1$^{EGFP/EGFP}$ (3-4 months; 2 male, 2 female), 4 middle-aged Cx3Cr1$^{EGFP/+}$ (12-15

months; 2 male, 2 female), and 4 middle-aged Cx3Cr1$^{EGFP/EGFP}$ mice (12-15 months; 2 male, 2 female). Histological examinations comparing microglia-deficient mice with controls utilized 3 young-adult Csf1r$^{\Delta FIRE/\Delta FIRE}$ mice (3-4 months, 2 females, 1 male) and 3 young-adult Csf1r$^{+/+}$ mice (3-4 months, 1 female, 2 males). Quantitative proteomic experiments included 4 young-adult (3-4 mo; 2 male, 2 female) and 4 aged (22-24 mo; 2 male, 2 female) wild-type mice. Behavioral testing and histological examinations utilized 18 young-adult (4 months; 9 male, 9 female) and 18 late-middle-aged (18 months; 9 male, 9 female) wild-type mice. All mice within a given experiment were housed in the same vivarium with a normal light/dark cycle and were provided *ad libitum* access to food and water. Experiments adhered to protocols approved by the Animal Care and Use Committee and UCLA.

Transcardial perfusion, immunohistochemistry, and histochemistry

Mice were deeply anesthetized in a covered beaker containing isofluorane and perfused transcardially with 1M phosphate buffered saline (PBS; pH 7.4) followed by ice-cold 4% paraformaldehyde (PFA) in 1M PBS. All perfusions were performed between 8:00 am and 12:00 pm to minimize the contribution that circadian changes may have on ECM, synapse, and microglial properties [52]. Brains were extracted immediately following perfusions and were allowed to post-fix for ~4 hours in 4% PFA and then stored in 1M PBS with 0.1% sodium azide until tissue sectioning.

Coronal brain sections were prepared using a vibratome in chilled 1M PBS solution and stored in 1M PBS with 0.1% sodium azide until histochemical labelling. Sections containing the ventral tegmental area (VTA) and nucleus accumbens (NAc) were selected using well-defined anatomical landmarks at 3 distinct anterior-posterior locations per mouse. Free-floating brain sections were briefly rinsed in 1M PBS (5 minutes) and then permeabilized and blocked in a solution of 1% bovine serum albumin (BSA) and 0.1% saponin for 1 hour. Sections were then incubated with a biotinylated HABP lectin (1:250; Sigma-Aldrich cat: 385911) in the 1% BSA

and 0.1% saponin block solution overnight at 4ºC with mild agitation. Sections were washed in 1M PBS (4x10 minutes) and then incubated with streptavidin-conjugated AlexaFluor-647 in the 1% BSA and 0.1% saponin block solution for 2 hours. The tissue underwent another 4x10 minute wash in 1M PBS, and then was blocked again in 5% normal donkey serum with no additional permeabilization agent for 1 hour and was then incubated overnight with mild agitation in a solution containing different combinations of goat anti-GFP (1:1000; Frontier Institute cat: GFP-go-Af1480), rabbit-anti-IBA1 (1:500; Wako cat: 019-19741), chicken anti-TH (1:500; Aves cat: TYH), rabbit anti-Homer2 (1:2000; Synaptic Systems cat: 160 003), and the biotinylated HABP lectin in 5% NDS solution. Sections were again washed in 1M PBS (4x10 minutes). Prior to secondary antibody incubation, all sections were treated with TrueBlack lipofuscin autofluorescence quencher (5%; Biotium cat: 23007) for 90 seconds followed by a 3x5 minute rinse in 1M PBS. Sections were then incubated in a secondary antibody solution containing combinations of chicken AlexaFluor-405 or chicken AlexaFluor-594, goat AlexaFluor-488, rabbit AlexaFluor-488 or rabbit AlexaFluor594, and streptavidin-conjugated AlexaFluor-647 in 5% NDS for 2 hours at room temperature with mild agitation. The sections were again washed in 1M PBS (4x10 minutes), were coverslipped (#1.5 thickness) and mounted using Aqua-Poly/Mount (Polysciences cat: 18606).

Image acquisition and analysis

Fixed-tissue was imaged using a Zeiss LSM-700 confocal microscope using a 63x objective at a z interval of 0.3 μm or a Leica STELLARIS 5 confocal microscope using 20x (z = 1.5) and 63x objectives (z = 0.3). For quantification of hyaluronan fibril deposition patterns, 63x images were imported into Fiji image analysis software and underwent a background subtraction (rolling-ball radius = 5) and de-speckling. The processed images were then binarized using the ‘MaxEntropy’ setting and hyaluronan fibril densities and sizes were assessed using the 3D Object Counter plugin in Fiji using a minimum pixel cutoff of 10.

Hyaluronan distribution regularity was quantified in the same images using the Fractal Dimension plugin in Fiji. Densities of homer2, putative hyaluronan-homer2 interactions, and hyaluronan and homer2 on TH-positive neurons were examined in 3-dimensions using custom-written MATLAB (Natick, MA) scripts.

Spatial correlations between microglia and hyaluronan were analyzed using 20x confocal stacks of histochemically labelled Cx3Cr1$^{EGFP/+}$ tissue. To obtain field-of-view correlations, hyaluronan and GFP channels were binarized after thresholding in Fiji and the proportion of hyaluronan and GFP pixels above threshold within each image was correlated. Microglia densities were calculated by manually counting microglial cell bodies within a z-stack using the Cell Counter plugin and then normalizing these counts by the volume of the image. More local measures of microglia-hyaluronan spatial correlations were assessed by overlaying a 10x10 grid over threshold 20x images using custom-written Fiji macros and the Pearson Correlation Coefficient of hyaluronan and microglial signal was calculated for each image using all 100 boxes of this grid.

Microglial morphological complexity was examined with 2-dimensional Sholl analysis using the SNT and Sholl Analysis plugin in Fiji[53]. Images containing IBA1 or GFP signal were first maximum intensity projected in the z dimension. A mark was placed in the center of each microglial soma and concentric radii were drawn from that point. The initial radius size was 7.5 µm and the step size of each radius after was 2.5 µm. The standard output values given by this plugin were used for analysis. Sholl intersection plots were made using MATLAB code.

Quantitative proteomics: sample preparation

Young and aged wild-type mice were anesthetized with isofluorane and perfused with 1M PBS. Brains were extracted and the midbrain and striatum were dissected using a scalpel, minced, triturated, washed in 1M PBS, and stored at -80°C until further processing. For

solubility-based fractionation experiments, the tissue was processed using protocols from Naba et al., 2015[28] using a compartment protein extraction kit (Millipore cat: 2145). Triturated brain tissue was thawed on ice for ~30 minutes before being homogenized in 2 ml/g of Buffer C (HEPES (pH 7.9), MgCl2, KCl, EDTA, Sucrose, Glycerol, Sodium OrthoVanadate) with protease inhibitors. This mixture was rotated on ice for 20 minutes and then spun at 20,000xg at 4ºC for 20 minutes. The supernatant was removed and stored at -80ºC until proteomic analysis. The pellet was washed in 4 ml/g of the same buffer (HEPES (pH 7.9), MgCl2, KCl, EDTA, Sucrose, Glycerol, Sodium OrthoVanadate) with protease inhibitors, rotated for 5 minutes at 4ºC, and spun at 20,000xg at 4ºC for 20 minutes. The supernatant was removed and discarded. The pellet was then incubated in 1ml/g of Buffer N (HEPES (pH 7.9), MgCl2, NAcl, EDTA, Glycerol, Sodium OrthoVanadate), rotated at 4ºC for 20 minutes, spun at 20,000xg for 20 minutes, and the supernatant was removed and stored at -80ºC until proteomic analysis. The pellet was then washed in 1ml/g of Buffer M (HEPES (pH 7.9), MgCl2, KCl, EDTA, Sucrose, Glycerol, Sodium deoxycholate, NP-40, Sodium OrthoVanadate), rotated at 4ºC for 20 minutes, spun at 20,000xg for 20 minutes, and the supernatant was removed and stored at -80ºC until proteomic analysis. The pellet was washed in 0.5 ml/g of buffer CS (Pipes (pH6.8), MgCl2, NAcl, EDTA, Sucrose, SDS, Sodium OrthoVanadate), rotated at 4ºC for 20 minutes, spun at 20,000xg for 20 minutes, and the supernatant was removed and stored at -80ºC until proteomic analysis. The final remaining insoluble pellet was also stored at -80ºC for proteomic analysis.

Chaotropic extraction and digestion experiments followed protocols from McCabe et al., 2023 [29], with the following modifications: Frozen samples were milled into powder in liquid nitrogen using a mortar and pestle. Approximately 5 mg of tissue was resuspended in a fresh prepared high-salt buffer (50 mM Tris-HCL, 3 M NaCl, 25 mM EDTA, 0.25% w/v CHAPS, pH 7.5) containing 1x protease inhibitor (Halt Protease Inhibitor, Thermo Scientific) at a concentration of 10 mg/ml. The samples were vortexed for 5 minutes and rotated at 4º C for 1

hour. The samples were then centrifuged for 20 minutes at 18,000xg at 4° C. The supernatants were discarded, and the pellets were resuspended in a high-salt buffer, vortexed for 5 minutes, and rotated again at 4° C for 1 hour. The samples were then recentrifuged for 15 minutes at 18,000xg at 4° C and the final pellets were used for proteomic analysis.

All samples were resuspended in equal volume of 8M Urea and 100mM Tris-Cl (pH 8). This was followed by reduction with TCEP and alkylation with IAA, followed by protein clean up with SP3 beads. Overnight digestion was done with trypsin and lysC enzymes. The peptides were cleaned using the SP3 protocol [54], followed by elution in 2% DMSO. Samples were dried using a speed vacuum, and the dried peptides were resuspended in 5% formic acid before being sent for liquid chromatotography with tandem mass spectrometry (LC-MS/MS).

Quantitative proteomics: analysis

MaxQuant software was used for peptide identification [55]. These algorithms use correlational analyses and graph theory to measure multiple mass measurements, and then integrate across these measurements and correct for linear and nonlinear mass offsets. Raw intensity data from each sample was batch corrected using a quantile normalization followed by a median centering procedure. This procedure uses an iterative algorithm to find the point that minimizes Euclidean distance to all features in the dataset and adjusts the distribution from each batch to this point. The intensity data of each identified protein was then summed across solubility fractions for each mouse and log2 normalized for analysis. To be included in the analysis, a protein needed to be detected in 75% or more of the samples within a brain region. Fold changes were calculated as the ratio of the aged signal relative to the young signal. Statistical significance was assessed using unpaired t-tests with an alpha-level of 0.05. Annotations for different protein classes were downloaded from publicly available online databases. ECM protein annotations were downloaded from the Matrisome project database [56],

innate immune system protein annotations from the InnateDB database [57], and synapse protein annotations from the SynGo database [58].

Quantitative proteomics: weighted gene correlation network analysis (WGCNA)

To examine relationships between synaptic, matrisome, and innate immune proteins, proteomic data underwent unsupervised clustering using Weighted Gene Correlation Network Analysis (WGCNA) in R [30]. Processed log2(intensity) data from the midbrain and striatum were used for network construction. One striatal sample from an aged female mouse was identified as an outlier and was removed from this analysis. WGCNA provides modules of covarying proteins that are agnostic to traits of the samples (i.e., age, region, sex). The distribution of synaptic, matrisome, and immune proteins across the protein modules was used to identify modules of interest for further analysis. Relationships between modules and external traits or protein abundance were examined using the module-trait relationship code provided in the WGCNA R package. Process enrichment analysis of the protein modules was conducted in Metascape [59] using default parameters.

Behavioral testing procedures

Behavioral testing was conducted in a large square open field (120 cm x 120 cm) with 35 cm high walls made from transparent Plexiglas. On one wall, there was a 20 cm x 20 cm opening where a start box equipped with a guillotine door was placed. This start location did not change across testing sessions. Mouse bedding was placed on the floor of the arena, and 2 intra-arena reference cues were placed at two fixed locations for the entire experiment. To also provide fixed distal landmarks to the mice, black corrugated plastic was placed on two adjacent walls in the arena, and white corrugated plastic was placed at the other two. Plexiglas dishes were filled with Sandtastik play sand (Sandtastik Products LLC, Port Colborne Ontario) and were used to plug 5TUL purified rodent tablets into (TestDiet; cat: 1811142; Quakertown, PA) to

engage foraging behavior. Identical feeders without reward pellets were used as distractor feeders to test goal-directed memory. The feeders were placed at 1 of 4 locations within the arena. All feeders were sham baited with powdered reward pellets (5% by weight). Mouse behavior was recorded using a 1.3 megapixel, low-illumination overhead camera (ELP; Shenzhen, Guangdong, China) and Bioserve Viewer software (Behavioral Instruments; Hillsborough, NJ).

Young-adult (3-4 months) and late-middle-aged (16-18 months) mice were ordered in 3 cohorts of 20 (5 young-adult female, 5 young-adult male, 5 late-middle-aged female, 5 late-middle-aged male). 12 mice from each cohort then underwent behavioral testing (6 young-adult, 6 middle-aged, equal male and female) and the other 8 lived with the behavior-trained mice but did not undergo testing (sedentary controls). Sample sizes were determined based on variability in pilot data and from published data on a similar task from which this one was derived[60].

Behavior-trained mice were handled daily for 1 week prior to testing. During week 1 of testing (habituation phase) mice were placed within the start box for ~2-3 minutes prior to the guillotine door opening to allow entry into the arena. A single sand well with 4 reward pellets was placed at one of the reward locations and the mice were allowed 5 minutes to explore the arena and retrieve the reward. This procedure was repeated daily for 5 sessions (1 session per day) for each mouse and the location of the rewarded feeder was changed daily and was counterbalanced within a day across mice. During weeks 2 and 3 (training phase), the mice again entered the arena via the start box and foraged for reward in a single sand well at one location in the arena for 5 minutes (encoding). Following a 30-minute delay period, mice reentered the arena with the rewarded feeder in the same location and 3 unrewarded feeders in the other locations for 2 minutes (retrieval). Note that this is a win-stay strategy. Again, the location of the rewarded feeder was changed daily for each mouse. Each mouse underwent 10 training sessions across 2 weeks of testing. In the final 2 weeks of testing (test phase), mice

repeated the encoding procedures described above. Following either 2- or 24-hour delays, mice underwent a probe test in which 4 unrewarded feeders were placed within the arena, 1 at the previously rewarded location. After 2 minutes the mice exited the arena through the guillotine door and the experimenter placed reward pellets in the previously rewarded location. The mice then reentered the arena and consumed the food reward to minimize extinction. Again, rewarded locations changed across sessions (4 sessions per delay; 1 session per day), and the 2- and 24-hour delays were interleaved to eliminate practice effects between the two conditions.

Behavioral testing data analysis

Mouse behavioral tracking was collected in 1-second timestamps and was used to determine the time of entry and exit to various zones of interest within the arena. These zones included the reward feeder locations, and a box that separated the arena's perimeter from the center. Data were exported from Bioserve Viewer software and loaded into Matlab for behavioral analysis using custom-written scripts. From these data the following output measures were derived: average running speed, start-box exit latency, proportion of time on the arena's perimeter, number of feeder visits, proportion of feeder visits to the correct feeder, the relative proportion of time in correct and incorrect feeders, and the number of errors prior to correct feeder visits. Note that because there were 4 foraging locations, chance performance during probe trials is 25% for proportional measures. For error measures, repeated errors to a specific unrewarded location were combined, making 1.5 errors to correct chance performance. Note that this estimate assumes that mice Probe trial data were used as the estimate of goal-directed memory function in these mice.

The temporal progression of the emergence of foraging behavior was tracked across sessions for each animal with a state-space modeling approach using Bernoulli observation models[61]. Mice were considered to have foraged if they consumed at least 1 of the 4 treats within the arena during the encoding sessions. Using this binary assessment (1 = consumed, 0

= non consumed), a learning curve, its 90% confidence bounds and the trial at which consistent foraging was observed were determined. This trial was defined as the point in which the lower bound of the 90% confidence interval exceeded chance (50%) and stayed above chance for the remainder of the experiment.

Statistical analysis

Statistical analyses were done using either MATLAB or R. Statistical significance of proteomic data was evaluated using unpaired t-tests. Immunohistochemical data was statistically analyzed using multi-way ANOVAs with Tukey's post-hoc tests where applicable, and behavior data was assessed using repeated-measures ANOVAs and unpaired t-tests. Relationships between anatomical variables and behavioral variables, or between different anatomical variables were assessed using robust regression analyses. In all cases the significance cutoff used was $p < 0.05$. Potential sex differences in hyaluronan, microglia, and excitatory synapse status were evaluated in all cases and no systematic differences between male and female mice were observed (see source data and statistics).

References

1. Burke, S. N. & Barnes, C. A. Neural plasticity in the ageing brain. *Nat Rev Neurosci* **7**, 30–40 (2006).
2. Tagliaferro, P. & Burke, R. E. Retrograde Axonal Degeneration in Parkinson Disease. *Journal of Parkinson's Disease* **6**, 1–15 (2016).
3. Terry, R. D. *et al.* Physical basis of cognitive alterations in alzheimer's disease: Synapse loss is the major correlate of cognitive impairment. *Annals of Neurology* **30**, 572–580 (1991).
4. Morrison, J. H. & Baxter, M. G. The ageing cortical synapse: hallmarks and implications for cognitive decline. *Nat Rev Neurosci* **13**, 240–250 (2012).
5. Dityatev, A., Schachner, M. & Sonderegger, P. The dual role of the extracellular matrix in synaptic plasticity and homeostasis. *Nat Rev Neurosci* **11**, 735–746 (2010).
6. Sorg, B. A. *et al.* Casting a Wide Net: Role of Perineuronal Nets in Neural Plasticity. *J. Neurosci.* **36**, 11459–11468 (2016).
7. Nguyen, P. T. *et al.* Microglial Remodeling of the Extracellular Matrix Promotes Synapse Plasticity. *Cell* **182**, 388-403.e15 (2020).
8. Lensjø, K. K., Christensen, A. C., Tennøe, S., Fyhn, M. & Hafting, T. Differential Expression and Cell-Type Specificity of Perineuronal Nets in Hippocampus, Medial Entorhinal Cortex, and Visual Cortex Examined in the Rat and Mouse. *eNeuro* **4**, (2017).
9. Dauth, S. *et al.* Extracellular matrix protein expression is brain region dependent. *Journal of Comparative Neurology* **524**, 1309–1336 (2016).
10. Fawcett, J. W. & Kwok, J. C. F. Proteoglycan Sulphation in the Function of the Mature Central Nervous System. *Frontiers in Integrative Neuroscience* **16**, (2022).
11. Foscarin, S., Raha-Chowdhury, R., Fawcett, J. W. & Kwok, J. C. F. Brain ageing changes proteoglycan sulfation, rendering perineuronal nets more inhibitory. *Aging (Albany NY)* **9**, 1607–1622 (2017).

12. Ueno, H. *et al.* Age-dependent and region-specific alteration of parvalbumin neurons and perineuronal nets in the mouse cerebral cortex. *Neurochemistry International* **112**, 59–70 (2018).
13. Badimon, A. *et al.* Negative feedback control of neuronal activity by microglia. *Nature* **586**, 417–423 (2020).
14. Cserép, C. *et al.* Microglia monitor and protect neuronal function through specialized somatic purinergic junctions. *Science* (2020) doi:10.1126/science.aax6752.
15. Miyamoto, A. *et al.* Microglia contact induces synapse formation in developing somatosensory cortex. *Nat Commun* **7**, 12540 (2016).
16. Paolicelli, R. C. *et al.* Synaptic Pruning by Microglia Is Necessary for Normal Brain Development. *Science* **333**, 1456–1458 (2011).
17. Schafer, D. P. *et al.* Microglia Sculpt Postnatal Neural Circuits in an Activity and Complement-Dependent Manner. *Neuron* **74**, 691–705 (2012).
18. Weinhard, L. *et al.* Microglia remodel synapses by presynaptic trogocytosis and spine head filopodia induction. *Nat Commun* **9**, 1228 (2018).
19. Venturino, A. *et al.* Microglia enable mature perineuronal nets disassembly upon anesthetic ketamine exposure or 60-Hz light entrainment in the healthy brain. *Cell Reports* **36**, 109313 (2021).
20. Soria, F. N. *et al.* Synucleinopathy alters nanoscale organization and diffusion in the brain extracellular space through hyaluronan remodeling. *Nat Commun* **11**, 3440 (2020).
21. Crapser, J. D. *et al.* Microglia facilitate loss of perineuronal nets in the Alzheimer's disease brain. *EBioMedicine* **58**, 102919 (2020).
22. Gray, D. T. *et al.* Retrosplenial cortex microglia and perineuronal net densities are associated with memory impairment in aged rhesus macaques. *Cerebral Cortex* bhac366 (2022) doi:10.1093/cercor/bhac366.

712 23. De Biase, L. M. *et al.* Local Cues Establish and Maintain Region-Specific Phenotypes of Basal Ganglia
713 Microglia. *Neuron* **95**, 341-356.e6 (2017).
714 24. Grabert, K. *et al.* Microglial brain region−dependent diversity and selective regional sensitivities to
715 aging. *Nature Neuroscience* **19**, 504–516 (2016).
716 25. Moca, E. N. *et al.* Microglia Drive Pockets of Neuroinflammation in Middle Age. *J. Neurosci.* **42**,
717 3896–3918 (2022).
718 26. Bäckman, L., Lindenberger, U., Li, S.-C. & Nyberg, L. Linking cognitive aging to alterations in
719 dopamine neurotransmitter functioning: Recent data and future avenues. *Neuroscience &*
720 *Biobehavioral Reviews* **34**, 670–677 (2010).
721 27. Dahl, M. J. *et al.* The integrity of dopaminergic and noradrenergic brain regions is associated with
722 different aspects of late-life memory performance. *Nat Aging* **3**, 1128–1143 (2023).
723 28. Naba, A., Clauser, K. R. & Hynes, R. O. Enrichment of Extracellular Matrix Proteins from Tissues and
724 Digestion into Peptides for Mass Spectrometry Analysis. *J Vis Exp* 53057 (2015) doi:10.3791/53057.
725 29. McCabe, M. C., Saviola, A. J. & Hansen, K. C. Mass Spectrometry-Based Atlas of Extracellular Matrix
726 Proteins across 25 Mouse Organs. *J. Proteome Res.* **22**, 790–801 (2023).
727 30. Langfelder, P. & Horvath, S. WGCNA: an R package for weighted correlation network analysis. *BMC*
728 *Bioinformatics* **9**, 559 (2008).
729 31. Hara, Y., Rapp, P. R. & Morrison, J. H. Neuronal and morphological bases of cognitive decline in aged
730 rhesus monkeys. *Age (Dordr)* **34**, 1051–1073 (2012).
731 32. Morgan, B. P. Complement in the pathogenesis of Alzheimer's disease. *Semin Immunopathol* **40**,
732 113–124 (2018).
733 33. Hong, S. *et al.* Complement and microglia mediate early synapse loss in Alzheimer mouse models.
734 *Science* **352**, 712–716 (2016).

735 34. Wilton, D. K. *et al.* Microglia and complement mediate early corticostriatal synapse loss and
736 cognitive dysfunction in Huntington's disease. *Nat Med* **29**, 2866–2884 (2023).
737 35. Wilson, E., Knudson, W. & Newell-Litwa, K. Hyaluronan regulates synapse formation and function in
738 developing neural networks. *Sci Rep* **10**, 16459 (2020).
739 36. Frischknecht, R. *et al.* Brain extracellular matrix affects AMPA receptor lateral mobility and short-
740 term synaptic plasticity. *Nat Neurosci* **12**, 897–904 (2009).
741 37. Schultz, W. Behavioral dopamine signals. *Trends in Neurosciences* **30**, 203–210 (2007).
742 38. Nyberg, L., Lövdén, M., Riklund, K., Lindenberger, U. & Bäckman, L. Memory aging and brain
743 maintenance. *Trends in Cognitive Sciences* **16**, 292–305 (2012).
744 39. Crapser, J. D., Arreola, M. A., Tsourmas, K. I. & Green, K. N. Microglia as hackers of the matrix:
745 sculpting synapses and the extracellular space. *Cell Mol Immunol* **18**, 2472–2488 (2021).
746 40. Rojo, R. *et al.* Deletion of a Csf1r enhancer selectively impacts CSF1R expression and development
747 of tissue macrophage populations. *Nat Commun* **10**, 3215 (2019).
748 41. Gyoneva, S. *et al.* Cx3cr1-deficient microglia exhibit a premature aging transcriptome. *Life Sci*
749 *Alliance* **2**, e201900453 (2019).
750 42. Gunner, G. *et al.* Sensory lesioning induces microglial synapse elimination via ADAM10 and
751 fractalkine signaling. *Nat Neurosci* **22**, 1075–1088 (2019).
752 43. Rivas-Fuentes, S. *et al.* CX3CL1 and CX3CR1 could be a relevant molecular axis in the
753 pathophysiology of idiopathic pulmonary fibrosis. *Int J Med Sci* **17**, 2357–2361 (2020).
754 44. Song, K. H., Park, J., Park, J. H., Natarajan, R. & Ha, H. Fractalkine and its receptor mediate
755 extracellular matrix accumulation in diabetic nephropathy in mice. *Diabetologia* **56**, 1661–1669
756 (2013).

757 45. Sugitani, K. *et al.* Hyaluronan degradation and release of a hyaluronan-aggrecan complex from
758 perineuronal nets in the aged mouse brain. *Biochimica et Biophysica Acta (BBA) - General Subjects*
759 **1865**, 129804 (2021).
760 46. Cargill, R. *et al.* Astrocytes in aged non-human primate brain gray matter synthesize excess
761 hyaluronan. *Neurobiol Aging* **33**, 830.e13-830.e24 (2012).
762 47. Soles, A. *et al.* Extracellular Matrix Regulation in Physiology and in Brain Disease. *Int J Mol Sci* **24**,
763 7049 (2023).
764 48. Chang, M. C. *et al.* Narp regulates homeostatic scaling of excitatory synapses on parvalbumin-
765 expressing interneurons. *Nat Neurosci* **13**, 1090–1097 (2010).
766 49. Pizzorusso, T. *et al.* Reactivation of Ocular Dominance Plasticity in the Adult Visual Cortex. *Science*
767 (2002) doi:10.1126/science.1072699.
768 50. Kim, A. *et al.* Reduced Fractalkine Levels Lead to Striatal Synaptic Plasticity Deficits in Huntington's
769 Disease. *Front Cell Neurosci* **14**, 163 (2020).
770 51. Jung, S. *et al.* Analysis of fractalkine receptor CX(3)CR1 function by targeted deletion and green
771 fluorescent protein reporter gene insertion. *Mol Cell Biol* **20**, 4106–4114 (2000).
772 52. Hayashi, Y. *et al.* The intrinsic microglial molecular clock controls synaptic strength via the circadian
773 expression of cathepsin S. *Sci Rep* **3**, 2744 (2013).
774 53. Ferreira, T. A. *et al.* Neuronal morphometry directly from bitmap images. *Nat Methods* **11**, 982–984
775 (2014).
776 54. Hughes, C. S. *et al.* Single-pot, solid-phase-enhanced sample preparation for proteomics
777 experiments. *Nat Protoc* **14**, 68–85 (2019).
778 55. Cox, J. & Mann, M. MaxQuant enables high peptide identification rates, individualized p.p.b.-range
779 mass accuracies and proteome-wide protein quantification. *Nat Biotechnol* **26**, 1367–1372 (2008).

780 56. Shao, X. *et al.* MatrisomeDB 2.0: 2023 updates to the ECM-protein knowledge database. *Nucleic*
781 *Acids Res* **51**, D1519–D1530 (2023).
782 57. Lynn, D. J. *et al.* InnateDB: facilitating systems-level analyses of the mammalian innate immune
783 response. *Molecular Systems Biology* **4**, 218 (2008).
784 58. Koopmans, F. *et al.* SynGO: An Evidence-Based, Expert-Curated Knowledge Base for the Synapse.
785 *Neuron* **103**, 217-234.e4 (2019).
786 59. Zhou, Y. *et al.* Metascape provides a biologist-oriented resource for the analysis of systems-level
787 datasets. *Nat Commun* **10**, 1523 (2019).
788 60. Takeuchi, T. *et al.* Locus coeruleus and dopaminergic consolidation of everyday memory. *Nature*
789 **537**, 357–362 (2016).
790 61. Smith, A. C. *et al.* Dynamic Analysis of Learning in Behavioral Experiments. *J. Neurosci.* **24**, 447–461
791 (2004).
792

Figures and Figure Legends

Figure 1. a) Schematic of the proteomic workflow. The midbrain and striatum of young adult (3-4 months) and aged (20-24 months) wild-type mice were dissected out. Tissue underwent a fractionation protocol that yielded multiple samples of proteins with decreasing solubility, and a final insoluble pellet. All samples were then sent for liquid chromatography with tandem mass spectrometry (LC-MS/MS) analysis. **b)** Average log2-transformed intensity values of core matrisome proteins were higher in aged mice (grey triangles) compared to young (black triangles) in both soluble and insoluble tissue fractions (black axis on left; $p = 0.023$), and higher in the midbrain compared to striatum ($p = 0.008$). Purple bars denote the number of core matrisome proteins detected in soluble and insoluble fractions for each region (purple axis on right). **c)** Volcano plots of all proteins pooled across solubility fractions for the midbrain and striatum. Dark blue dots denote individual core matrisome proteins detected in each region. Fold-changes were calculated with respect to the aged mice (positive values indicate greater with age). **d)** Log2-transformed intensity values (black axis on left) and fold changes (purple axis on right) for all collagens detected in the midbrain and striatum of young and aged mice. **e)** Abundances and fold changes for all detected glycoproteins in the midbrain and striatum. The dotted purple line represents a fold-change of 0. **f)** Abundances and fold changes for all detected proteoglycans in the midbrain and striatum. **g)** Venn diagram depicting all differentially expressed core matrisome proteins found specifically in the midbrain (pink), striatum (beige), as well as those differentially expressed in both regions. Statistical comparisons were made using multi-way ANOVA or unpaired t-tests. * $p < 0.05$

Figure 2. a) Left: dendrogram generated by Weighted Gene Coexpression Network Analysis (WGCNA) of all midbrain and striatal proteomic samples. Right: pie charts of classified core matrisome and innate immune protein distribution across modules. Only percentage values above 10% are denoted. **b)** Module eigengenes for each of the brown, yellow, tan, and

turquoise modules for each sample. One aged female was classified as an outlier by the WGCNA and was removed from subsequent analyses. **c)** Enriched biological terms associated with brown, yellow, tan, and turquoise module proteins. **d)** Heatmaps representing correlations between brown, yellow, tan, and turquoise module eigengenes and abundances of specific extracellular matrix proteoglycans, complement proteins, GABAergic receptors, glutamatergic receptors, and synaptic scaffolding proteins (* $p < 0.05$). **e)** Network plots of process and pathway enrichment terms associated with all tan/yellow/brown module (left) and turquoise module (right) proteins whose abundances were modulated by age ($p < 0.05$) in the midbrain and striatum.

Figure 3. a) The ECM scaffold hyaluronan (HA) was analyzed in two critical regions of the mesolimbic dopamine system, the ventral tegmental area (VTA) and nucleus accumbens (NAc). **b)** Example photomicrographs of histochemically labelled hyaluronan in the VTA and NAc of a young-adult (4 months) and late-middle-aged (18 months) mouse (left panels). Middle panels show zoomed in images of the areas within the yellow squares in the left panels. The right panels depict binarized images of the hyaluronan matrix used for quantification. **c-e)** Boxplots depicting **c)** hyaluronan fibril densities, **d)** median hyaluronan fibril sizes, and **e)** hyaluronan distribution regularity (Fractal Dimension plugin – Fiji) in the VTA and NAc of young-adult (black) and late-middle-aged (grey) mice. Higher fractal dimension values (D') indicate more spatial regularity of the hyaluronan matrix. Hyaluronan fibril density, median size, and distribution regularity were greater in the VTA compared to NAc (Density: $p < 0.001$; Size: $p < 0.001$; Regularity: $p < 0.001$). Late-middle-aged mice exhibited significantly greater VTA hyaluronan fibril density ($p = 0.027$) and distribution regularity ($p = 0.0009$) **f)** Left panels: example photomicrographs of histochemically labelled hyaluronan, immunohistochemically labelled homer2 (excitatory postsynaptic puncta) and tyrosine hydroxylase (TH; dopaminergic neurons/processes) in the VTA and NAc of a young-adult wild-type mouse. Right panels:

zoomed in images of the fields of view depicted by the white squares in the left panels. Arrows highlight putative hyaluronan-homer2 colocalized puncta and small squares depict homer2 puncta not associated with hyaluronan. **g)** Homer2 densities were greater in the NAc compared to the VTA ($p = 0.0036$), but not different between young-adult and late-middle-aged mice in either region. **h)** Schematic hyaluronan-homer2 proximity analysis. **i)** Densities of homer2 within 0.5 µm of hyaluronan was significantly lower in images where 1 channel was rotated by 90 degrees in both the VTA ($p < 0.0001$) and NAc ($p = 0.0065$), indicating that spatial relationships between the two are not random in these brain regions. Statistical comparisons were made using multi-way ANOVA or paired t-tests. * $p < 0.05$; ** $p < 0.01$, *** $p < 0.001$

Figure 4. a) Schematic depicting the foraging arena with proximal (fixed objects within arena) and distal (grey and black walls) reference landmarks, a start box equipped with a guillotine door, and overhead tracking of mouse behavior (yellow). **b)** Schematic depiction of the training and test phases of reward-based foraging paradigm. **c)** The number of feeder visits during encoding trials increased across sessions in both young-adult (4 months; black) and late-middle-aged (18 months; grey) mice ($p = 0.0016$). **d)** The number of trials to consistent foraging behavior. ($p = 0.32$). **e)** The proportion of reward feeder visits across training sessions. A greater proportion of feeder visits were to the rewarded feeder in older mice ($p = 0.004$). **f)** Average running speed, **g)** the latency to exit the start box, and **h)** proportion of time on the perimeter of the arena. **i)** The proportion of correct feeder visits during probe trials at 2- and 24-hour delays (left and middle), and the within-subject difference measure (24 hr. - 2 hr.; right). Middle-aged mice made significantly fewer correct feeder visits at 24 hours compared to 2 hours ($p = 0.02$), whereas the performance of the young-adult mice was similar between the two conditions. **j)** The number of errors to correct feeder visits during probe trials at 2- and 24-hour delays (left and middle), and the within subject difference measure (24 hr. – 2 hr.). Middle-aged mice made more errors at the 24-hour condition compared to young ($p = 0.003$) and made

significantly more errors at 24 hours compared to 2 hours. ($p = 0.005$). Statistical comparisons were made using 2-way ANOVA, repeated-measures ANOVA, or unpaired t-tests. * $p < 0.05$; ** $p < 0.01$.

Figure 5. a) Hyaluronan and homer2 were assessed in the VTA of young-adult (4 months) and late-middle-aged (18 months) behavior-trained mice and sedentary controls. **b)** Top: example photomicrographs of histochemically labelled hyaluronan from a sedentary and behavior-trained 18-month-old mouse. Bottom: binarized images of the hyaluronan matrix used for quantification. **c)** Boxplots depicting VTA hyaluronan fibril densities in young-adult sedentary (black) and behavior-trained (dark grey) mice and late-middle-aged sedentary (light grey) and behavior-trained mice (white). Behavior-trained mice exhibited lower hyaluronan densities relative to controls ($p = 0.0005$), and behavior-trained middle-aged mice had lower hyaluronan levels relative to sedentary ($p = 0.0047$). **d)** Relationship between VTA hyaluronan fibril densities and performance on reward-based foraging task (proportion of correct feeder visits difference measure). A significant negative relationship was observed in middle-aged mice ($p = 0.006$). **e)** Example photomicrographs of immunolabelled homer2 from a sedentary and behavior-trained 18-month-old mouse. **f)** Boxplots of VTA homer2 densities in young-adult sedentary and behavior-trained mice and late-middle-aged sedentary and behavior-trained mice. Behavior-trained mice exhibited higher homer2 densities relative to controls ($p = 0.03$). **g)** Relationship between VTA homer2 densities and performance on reward-based foraging task. Significant negative relationships were observed across all mice (purple; $p = 0.0045$) and in middle-aged mice ($p = 0.047$). **h)** Schematic of analysis strategy to examine hyaluronan and homer2 on tyrosine-hydroxylase (TH-homer2) expressing dopamine neurons. **i)** Boxplots depicting TH-homer2 densities in young-adult sedentary (black) and behavior-trained (dark grey) mice and late-middle-aged sedentary (light grey) and behavior-trained mice (white). **j)** Relationship between TH-homer2 densities and performance on reward-based foraging task. A significant

negative relationship was observed in middle-aged mice (grey; $p = 0.039$). **k)** Scatter plots of TH-hyaluronan densities plotted against TH-homer2 densities in sedentary and behavior-trained mice. No significant relationships were observed in sedentary mice, but significant positive relationships were seen in behavior-trained at both ages (young: $p = 0.0016$; middle-aged: $p = 0.014$). Statistical comparisons were made using 2-way ANOVA and robust regression analyses. * $p < 0.05$; ** $p < 0.01$; *** $p < 0.001$.

Figure 6. a) IBA1-positive microglia in the ventral tegmental area (VTA) and nucleus accumbens (NAc) of behavior-trained mice. **b)** VTA and NAc microglia densities in young-adult and middle-aged mice that underwent behavioral training. Greater microglia densities were observed in the NAc compared to VTA ($p < 0.0001$), and in the VTA, microglia densities were greater in middle-aged mice ($p < 0.0001$). **c)** Relationship between VTA and NAc microglia densities and performance on reward-based foraging task (proportion of correct feeder visits difference measure). In the VTA, significant negative relationships were observed across all mice (purple; $p = 0.00017$) and in middle-aged mice (grey; $p = 0.004$), whereas in the NAc, significant positive relationships were observed (all: $p = 0.038$; middle-aged: $p = 0.036$). **d)** Example high-magnification (63x) photomicrographs of immunolabelled IBA1-positive microglia from a sedentary and behavior-trained 18-month-old mouse. **e)** Boxplots of VTA microglia tissue coverage in young-adult sedentary and behavior-trained mice and late-middle-aged sedentary and behavior-trained mice. **f)** Relationship between VTA microglia tissue coverage and performance on reward-based foraging task. A significant negative relationship was observed across all mice (purple; $p = 0.01$). **g)** Scatter plots of microglia tissue coverage and hyaluronan fibril densities and **h)** sizes for sedentary and behavior-trained mice. Significant positive relationships were observed in middle-aged sedentary ($p = 0.0094$) and behavior-trained mice ($p = 0.0078$). Statistical comparisons were made using 2-way ANOVA and robust regression analyses. * $p < 0.05$; ** $p < 0.01$; *** $p < 0.001$.

Figure 7. a) Top row: example photomicrographs of 20x confocal images of histochemically labelled hyaluronan (HA) and GFP-labelled microglia from the ventral tegmental area (VTA) of a young-adult (3 months) $Cx3Cr1^{EGFP/+}$ mouse. Middle-row: thresholded images of GFP and hyaluronan used for analysis. Bottom row: zoom in on the field-of-view depicted by the yellow rectangles. **b)** Scatter plots of VTA and nucleus accumbens (NAc) field-of-view microglial tissue coverage (% FOV) plotted against field-of-view hyaluronan tissue coverage for young-adult (3-4 months; black), middle-aged (12-17 months; dark grey), and aged (18-22 months; light grey) $Cx3Cr1^{EGFP/+}$ mice. Asterisks depict significant correlations ($p < 0.05$). **c)** Left: example of grid overlaid on 20x confocal images to determine spatial correlations between hyaluronan and GFP signals. Images on the bottom are zoom-ins of the areas depicted by the yellow squares on the top. Right: The Pearson's correlation coefficient was calculated for each image by correlating the hyaluronan and GFP signals within each square. The top scatter plot is an example from the VTA and the bottom from the NAc. **d)** Correlation coefficients of spatial relationships between hyaluronan and microglia in the VTA and NAc. Boxplots denote the middle 50% of the data and horizontal lines denote the median of each distribution. Hyaluronan-microglia spatial correlations were significantly lower in the NAc compared to the VTA ($p = 0.0004$). Statistical comparisons were made using linear regression or multi-way ANOVA. * $p < 0.05$; ** $p < 0.01$.

Figure 8. a) Hyaluronan matrix deposition and homer2 densities were assessed in young-adult (3 months) Csf1r$^{\Delta FIRE/\Delta FIRE}$ mice in which microglia are constitutively depleted, and Csf1r$^{+/+}$ control mice. **b)** Hyaluronan fibril densities and **c)** homer2 puncta densities in the VTA of Csf1r$^{+/+}$ (black triangles) and Csf1r$^{\Delta FIRE/\Delta FIRE}$ (grey triangles) mice. Hyaluronan densities were greater in Csf1r$^{\Delta FIRE/\Delta FIRE}$ mice compared to Csf1r$^{+/+}$ ($p = 0.007$). **d)** VTA hyaluronan and homer2 densities were also examined in young-adult (3-4 months) and early-middle-aged (12-15 months) Cx3Cr1-heterozygous (Cx3Cr1$^{EGFP/+}$) and Cx3Cr1-knockout (Cx3Cr1$^{EGFP/EGFP}$) mice. **e)** Middle-aged Cx3Cr1$^{EGFP/EGFP}$ mice exhibited lower hyaluronan fibril densities compared to young whereas hyaluronan densities in Cx3Cr1$^{EGFP/+}$ mice exhibited a modest increase with age (interaction effect: $p=0.023$). **f)** Homer 2 puncta densities were lower in both Cx3Cr1$^{EGFP/+}$ and Cx3Cr1$^{EGFP/EGFP}$ mice by early middle age ($p = 0.0003$). **g)** Putative microglia engulfment of hyaluronan and homer2 was also examined in Cx3Cr1$^{EGFP/+}$ and Cx3Cr1$^{EGFP/EGFP}$ mice. **h)** Putative microglia-hyaluronan engulfment and **i)** microglia-homer2 engulfment in Cx3Cr1$^{EGFP/+}$ and Cx3Cr1$^{EGFP/EGFP}$ mice. Fewer homer2 puncta were found within GFP-positive microglia in early-middle-aged Cx3Cr1$^{EGFP/+}$ and Cx3Cr1$^{EGFP/EGFP}$ mice ($p = 0.003$). Statistical comparisons were made using 2-way ANOVA, unpaired t-test, or robust regression analyses. * $p < 0.05$; ** $p < 0.01$, α = age x genotype interaction effect.

Extended Data Figures and Figure Legends

Extended Data Figure 1. **a)** The midbrain and striatum of young-adult (3 months) mice were dissected and underwent either chaotropic extraction and digestion (n = 4) or solubility-based tissue fractionation (n=4) protocols. **b)** Comparison of the number of core matrisome proteins demonstrates that slightly more individual ECM proteins were detected using solubility-based fractionation. **c)** Log2-transformed intensity values (*black axis on left*) and fold changes (*purple axis on right*) for all midbrain and striatum core matrisome proteins detected using chaotropic extraction and digestion (black) and solubility-based tissue fractionation (grey). Positive fold-change indicates higher abundance with solubility-based fractionation.

Extended Data Figure 2. **a)** Log2-transformed intensity values (black axis on left) and fold changes (purple axis on right) for all ECM-degradative enzymes and **b)** ECM protease inhibitors and ECM crosslinking proteins in the midbrain and striatum of young (black) and aged (grey) mice. The dotted purple line represents a fold-change of 0. **c)** Average of all log2 intensity values of all ECM degradative enzymes and **d)** ECM protease inhibitors and ECM crosslinking proteins in the midbrain and striatum within individual mice. * $p < 0.05$.

Extended Data Figure 3. Heatmaps representing correlations between brown, yellow, tan, and turquoise module eigengenes and abundances of specific innate immune proteins separated by functional classification (ribonuclear proteins, kinases and phosphatases, ubiquitin-associated proteins, mitochondrial proteins, complement proteins, and other miscellaneous innate immune proteins). * $p < 0.05$.

Extended Data Figure 4. **a)** Most structural synapse proteins were found in the brown or yellow modules as seen in pie chart representing the distribution of synapse receptors and scaffold proteins across WGCNA modules. **b)** Log2-transformed intensity values (black axis on left) and fold changes (purple axis on right) for all inhibitory synapse and **c)** excitatory synapse proteins

detected in the midbrain and striatum of young (black) and aged (grey) mice. The dotted purple line represents a fold-change of 0. **d)** Log2-transformed intensity values of all synaptic scaffolding proteins and **e)** synaptic vesicle transporter proteins detected.

Extended Data Figure 5. **a)** Example photomicrograpghs of histochemically labelled hyaluronan (HA), tyrosine hydroxylase(TH)-positive dopaminergic neurons, and IBA1-positive microglia in the substantia nigra pars compacta (SNc). **b**) SNc hyaluronan fibril densities, sizes, and distribution regularity were not different between young-adult (4 months) and late-middle-aged mice (18 months).**c)** Example photomicrograpghs of histochemically labelled hyaluronan (HA) in the medial prefrontal cortex (mPFC; left) and retrosplenial cortex (RSC; right) from a 4-month-old and 18-month-old mouse. **d)** Hyaluronan fibril densities were also not different in the mPFC and RSC of young-adult (4 months) and late-middle-aged mice (18 months).

Extended Data Figure 6. **a)** Behavioral raster plots of treats eaten (top) and feeder visits (bottom) during encoding across sessions used for hidden Markov modeling of foraging behavior. **b)** Representative learning curves from hidden Markov modeling for a young-adult and late-middle-aged mouse. **c)** The modeled estimates of the percent of sessions foraged and the probability of foraging using data of treats eaten and **d)** feeder visits data for young-adult (4 months; black) and late-middle-aged (18 months; grey) mice. **e)** The number of treats eaten of 4 across all encoding sessions for young-adult and middle-aged mice. **f)** The duration of feeder visits increased across sessions. **g)** The area covered across sessions for young-adult and late-middle-aged mice. **h)** The proportion of feeder visits to the correct feeder location during training sessions for young-adult and late-middle-aged mice. **i)** Variability in running speeds for young-adult and late-middle-aged mice. Middle-aged mice exhibited lower running speed variability compared to young. * $p < 0.05$, ** $p < 0.01$.

Extended Data Figure 7. **a)** Boxplots depicting hyaluronan fibril densities, size, and distribution regularity in young-adult sedentary (black) and behavior-trained (dark grey) mice and late-

middle-aged sedentary (light grey) and behavior-trained mice (white) in the ventral tegmental area (VTA), **b)** substantia nigra pars compacta (SNc), and **c)** nucelus accumbens (NAc). **d)** Boxplots depicting hyaluronan fibril densities in the medial prefrontal cortex (mPFC), retrosplenial cortex (RSC), and CA3 region of the hippocampus of young-adult sedentary and behavior-trained mice and late-middle-aged sedentary and behavior-trained mice. ** $p < 0.01$, *** $p < 0.001$

Extended Data Figure 8. a) Left: example photomicrograph of histochemically labelled tyrosine hydroxylase(TH)-positive neurons and hyaluronan in the VTA of a middle-aged mouse. Right: peri-TH ROIs (magenta) used to index hyaluronan fragment on dopamine neurons (TH-hyaluronan; yellow). **b)** Left: Boxplots depicting TH-hyaluronan fibril densities normalized to the TH signal in young-adult sedentary (black) and behavior-trained (dark grey) mice and late-middle-aged sedentary (light grey) and behavior-trained mice (white). Behavior-trained mice exhibited lower TH-hyaluronan densities relative to controls. Right: Relationship between TH-hyaluronan fibril densities and performance on reward-based foraging task (proportion of correct feeder visits difference measure). **c)** Left: example photomicrograph of an IBA1-positive microglia cell body and proximal branches and hyaluronan in the VTA of a middle-aged mouse. Right: IBA1 ROI used to examine hyaluronan fragments in contact with microglia (IBA1-hyaluronan). **d)** Left: Boxplots depicting IBA1-hyaluronan fibril densities normalized to the IBA1 signal in young-adult sedentary (black) and behavior-trained (dark grey) mice and late-middle-aged sedentary (light grey) and behavior-trained mice (white). Behavior-trained mice exhibited lower IBA1-hyaluronan densities relative to controls. Right: Relationship between IBA1-hyaluronan fibril densities and performance on reward-based foraging task (proportion of correct feeder visits difference measure). **e)** Relationship between VTA and NAc microglia density and difference measures of the number of errors made during 2 and 24-hour probe trials. **f)** Scatter plots of hyaluronan fibril densities and homer2 densities for all co-labelled fields-of-view in

sedentary and behavior-trained mice. A significant positive relationship was observed in behavior-trained middle-aged mice. * $p < 0.05$, ** $p < 0.01$

Extended Data Figure 9. **a)** 2-dimensional Sholl analysis was performed on ventral tegmental area (VTA) and nucleus accumbens (NAc) IBA1-positive microglia in young-adult (4 months) and late-middle-aged (18 months) mice. **b)** Sholl intersection plots for VTA and NAc microglia for young-adult and late-middle-aged mice. **c)** Sholl analysis output measures for VTA and **d)** NAc microglia. These include the maximum Sholl radius with a microglial intersection (max radius), the sum of microglia intersections across radii (sum of intersections), Sholl branching index, and Sholl decay. **e)** Example photomicrographs of GFP-positive microglia in the VTA of 12-month-old Cx3Cr1$^{EGFP/+}$(het) and Cx3Cr1$^{EGFP/EGFP}$ (KO) mice. **f)** Sholl intersection plots for VTA microglia from young-adult (3-4 months) and early-middle-aged Cx3Cr1-het and Cx3Cr1-KO mice. **g)** Output measures for VTA microglia from young-adult (3-4 months) and early-middle-aged Cx3Cr1-het and Cx3Cr1-KO mice. * $p < 0.05$, ** $p < 0.01$

Supplemental Figures and Figure Legends

Figure S1. a) Sample clustering dendrogram of midbrain and striatal proteomic samples. One outlier (aged female) was detected using the default height cutoff of 100 and was subsequently removed from analysis. **b)** Heatmap depicting the Topological Overlap Matrix of all proteins. Protein dendrograms and module assignments are shown above and to the left of the heatmap. Darker colors indicate a higher degree of overlap. **c)** Analysis of scale independence and mean connectivity for various soft-threshold powers. **d)** Eigengene adjacency map for WGCNA modules. Red color indicates higher eigengene adjacency and blue indicates low adjacency. **e)** Module-trait relationships between module eigengenes and the region, age, and sex of the samples. * $p < 0.05$.

Figure S2. **a)** Colocalization of ventral tegmental area (VTA) and nucleus accumbens (NAc) hyaluronan (yellow) and homer 2 (cyan) was assessed using custom MATLAB scripts. Puncta highlighted in red in the right-hand panels are the colocalized puncta observed in these example photomicrographs. **b)** The density of colocalized hyaluronan-homer2 puncta in the VTA and NAc of young-adult (4 months; green) and late-middle-aged (18 months; purple) mice. No differences were observed as a function or age or brain region. **c)** The proportion of synapses colocalized with hyaluronan and **d)** the proportion of hyaluronan fibrils colocalized with homer2 were also not different as a function of age or brain region.

Figure S3. a) Left: Example photomicrographs of histochemically labelled hyaluronan (HA) and tyrosine hydroxylase (TH) in the ventral tegmental area of a young-adult (3-4 months) and aged (22 months) $Cx3Cr1^{EGFP/+}$ mice. Right: 3-dimensional Imaris reconstructions of hyaluronan networks and TH neurons in the example images. **b)** Average VTA hyaluronan fibril sizes in contact with TH-positive neurons. * $p < 0.05$.

Figure S4. a) Example photomicrographs of histochemically labelled hyaluronan (HA) and homer2 in the nucleus accumbens of a young-adult (3 months) $Csf1r^{\Delta FIRE/\Delta FIRE}$ mouse. **b)** NAc hyaluronan fibril and **c)** homer2 puncta densities in $Csf1r^{+/+}$ (black triangles) and $Csf1r^{\Delta FIRE/\Delta FIRE}$ (grey triangles) mice. **d)** Example photomicrographs of histochemically labelled hyaluronan and homer2 in the NAc of young-adult (3-4 months) and early-middle-aged (12-15 months) Cx3Cr1-heterozygous ($Cx3Cr1^{EGFP/+}$) and Cx3Cr1-knockout ($Cx3Cr1^{EGFP/EGFP}$) mice. **e)** NAc hyaluronan fibril and **f)** homer2 puncta densities in young-adult and early-middle-aged Cx3Cr1-heterozygous and Cx3Cr1-knockout mice. **g)** Depiction of putative microglia engulfment of hyaluronan and homer2 in the NAc. **h)** Putative microglia-hyaluronan engulfment and **i)** microglia-homer2 engulfment in $Cx3Cr1^{EGFP/+}$ and $Cx3Cr1^{EGFP/EGFP}$ mice. * $p < 0.05$

Figure S5. a) Density **b)** size and **c)** distribution regularity of hyaluronan fibrils detected in the ventral tegmental area (VTA) and nucleus accumbens (NAc) of young-adult (4 months) and late-middle-aged mice (18 months) plotted with male and female mice distinguished by color (blue: male; red: female). The lower panels show boxplots with male and female mice distinguished by color of **d)** homer2 densities, **e)** colocalized hyaluronan-homer2 puncta, **f)** hyaluronan-homer2 puncta within 0.5 µm, and **g)** paired plots of hyaluronan-homer2 puncta within 0.5 µm compared to images in which 1 channel was rotated. * $p < 0.05$, ** $p < 0.01$

Figure S6. a) Body weight at time of perfusion of young-adult sedentary (black) and behavior-trained (dark grey) mice and late-middle-aged sedentary (light grey) and behavior-trained mice (white). ** $p < 0.01$

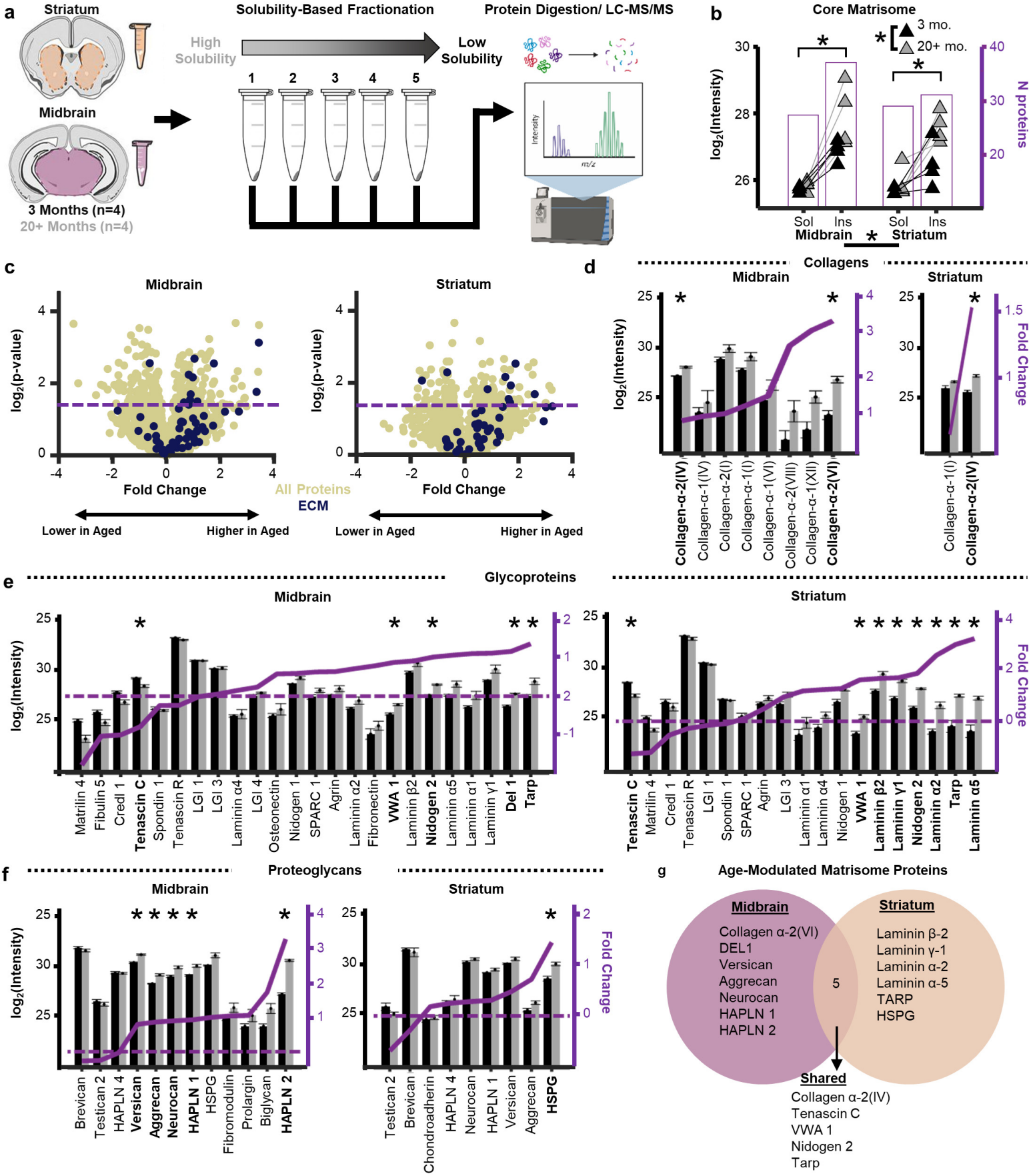
a
Striatum
Midbrain
3 Months (n=4)
20+ Months (n=4)
Solubility-Based Fractionation
High Solubility
Low Solubility
1
2
3
4
5
Protein Digestion/ LC-MS/MS
Intensity
m/z
b
Core Matrisome
3 mo.
20+ mo.
log2(Intensity)
N proteins
Sol
Ins
Sol
Ins
Midbrain
Striatum
c
Midbrain
Striatum
log2(p-value)
Fold Change
All Proteins
ECM
Lower in Aged
Higher in Aged
d
Collagens
Midbrain
Striatum
log2(Intensity)
Fold Change
Collagen-α-2(IV)
Collagen-α-1(IV)
Collagen-α-2(I)
Collagen-α-1(I)
Collagen-α-1(VI)
Collagen-α-2(VIII)
Collagen-α-1(XII)
Collagen-α-2(VI)
Collagen-α-1(I)
Collagen-α-2(IV)
e
Glycoproteins
Midbrain
Striatum
log2(Intensity)
Fold Change
Matrilin 4
Fibulin 5
Credl 1
Tenascin C
Spondin 1
Tenascin R
LGI 1
LGI 3
Laminin α4
LGI 4
Osteonectin
Nidogen 1
SPARC 1
Agrin
Laminin α2
Fibronectin
VWA 1
Laminin β2
Nidogen 2
Laminin α5
Laminin α1
Laminin γ1
Del 1
Tarp
Tenascin C
Matrilin 4
Credl 1
Tenascin R
LGI 1
Spondin 1
SPARC 1
Agrin
LGI 3
Laminin α1
Laminin α4
Nidogen 1
VWA 1
Laminin β2
Laminin γ1
Nidogen 2
Laminin α2
Tarp
Laminin α5
f
Proteoglycans
Midbrain
Striatum
log2(Intensity)
Fold Change
Brevican
Testican 2
HAPLN 4
Versican
Aggrecan
Neurocan
HAPLN 1
HSPG
Fibromodulin
Prolargin
Biglycan
HAPLN 2
Testican 2
Brevican
Chondroadherin
HAPLN 4
Neurocan
HAPLN 1
Versican
Aggrecan
HSPG
g
Age-Modulated Matrisome Proteins
Midbrain
Collagen α-2(VI)
DEL1
Versican
Aggrecan
Neurocan
HAPLN 1
HAPLN 2
5
Striatum
Laminin β-2
Laminin γ-1
Laminin α-2
Laminin α-5
TARP
HSPG
Shared
Collagen α-2(IV)
Tenascin C
VWA 1
Nidogen 2
Tarp

Figure 1

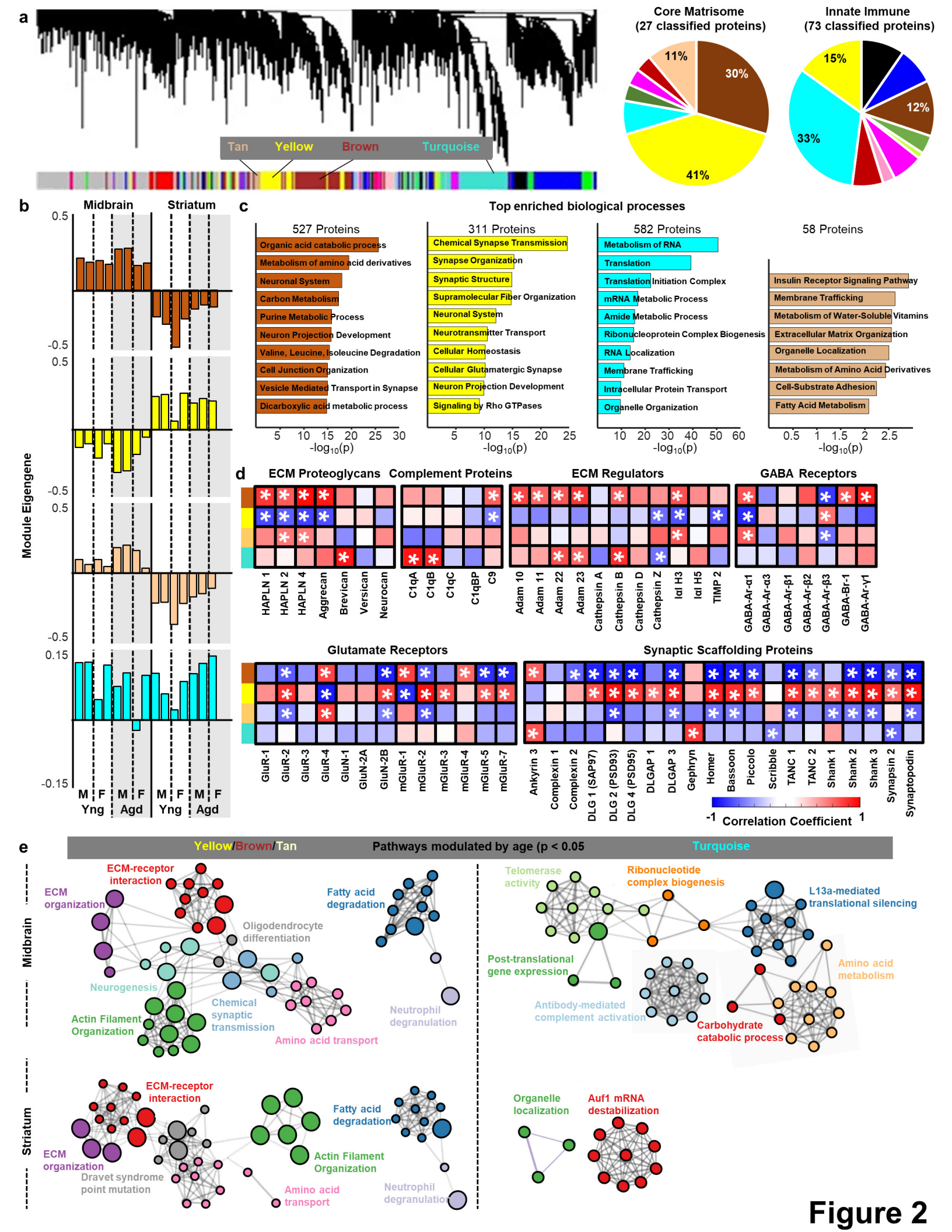
a
Tan
Yellow
Brown
Turquoise
Core Matrisome
(27 classified proteins)
30%
41%
11%
Innate Immune
(73 classified proteins)
15%
12%
33%
b
Midbrain
Striatum
Module Eigengene
0.5
-0.5
0.15
-0.15
M F M F M F M F
Yng Agd Yng Agd
c
Top enriched biological processes
527 Proteins
Organic acid catabolic process
Metabolism of amino acid derivatives
Neuronal System
Carbon Metabolism
Purine Metabolic Process
Neuron Projection Development
Valine, Leucine, Isoleucine Degradation
Cell Junction Organization
Vesicle Mediated Transport in Synapse
Dicarboxylic acid metabolic process
311 Proteins
Chemical Synapse Transmission
Synapse Organization
Synaptic Structure
Supramolecular Fiber Organization
Neuronal System
Neurotransmitter Transport
Cellular Homeostasis
Cellular Glutamatergic Synapse
Neuron Projection Development
Signaling by Rho GTPases
582 Proteins
Metabolism of RNA
Translation
Translation Initiation Complex
mRNA Metabolic Process
Amide Metabolic Process
Ribonucleoprotein Complex Biogenesis
RNA Localization
Membrane Trafficking
Intracellular Protein Transport
Organelle Organization
58 Proteins
Insulin Receptor Signaling Pathway
Membrane Trafficking
Metabolism of Water-Soluble Vitamins
Extracellular Matrix Organization
Organelle Localization
Metabolism of Amino Acid Derivatives
Cell-Substrate Adhesion
Fatty Acid Metabolism
-log10(p)
d
ECM Proteoglycans
HAPLN 1
HAPLN 2
HAPLN 4
Aggrecan
Brevican
Versican
Neurocan
Complement Proteins
C1qA
C1qB
C1qC
C1qBP
C9
ECM Regulators
Adam 10
Adam 11
Adam 22
Adam 23
Cathepsin A
Cathepsin B
Cathepsin D
Cathepsin Z
Itl H3
Itl H5
TIMP 2
GABA Receptors
GABA-Ar-α1
GABA-Ar-α3
GABA-Ar-β1
GABA-Ar-β2
GABA-Ar-β3
GABA-Br-1
GABA-Ar-γ1
Glutamate Receptors
GluR-1
GluR-2
GluR-3
GluR-4
GluN-1
GluN-2A
GluN-2B
mGluR-1
mGluR-2
mGluR-3
mGluR-4
mGluR-5
mGluR-7
Synaptic Scaffolding Proteins
Ankyrin 3
Complexin 1
Complexin 2
DLG 1 (SAP97)
DLG 2 (PSD93)
DLG 4 (PSD95)
DLGAP 1
DLGAP 3
Gephryn
Homer
Bassoon
Piccolo
Scribble
TANC 1
TANC 2
Shank 1
Shank 2
Shank 3
Synapsin 2
Synaptopodin
-1
Correlation Coefficient
1
e
Yellow/Brown/Tan
Pathways modulated by age (p < 0.05
Turquoise
Midbrain
ECM-receptor interaction
ECM organization
Fatty acid degradation
Oligodendrocyte differentiation
Neurogenesis
Chemical synaptic transmission
Actin Filament Organization
Amino acid transport
Neutrophil degranulation
Striatum
ECM-receptor interaction
Fatty acid degradation
ECM organization
Actin Filament Organization
Dravet syndrome point mutation
Amino acid transport
Neutrophil degranulation
Telomerase activity
Ribonucleotide complex biogenesis
L13a-mediated translational silencing
Post-translational gene expression
Amino acid metabolism
Antibody-mediated complement activation
Carbohydrate catabolic process
Organelle localization
Auf1 mRNA destabilization

Figure 2

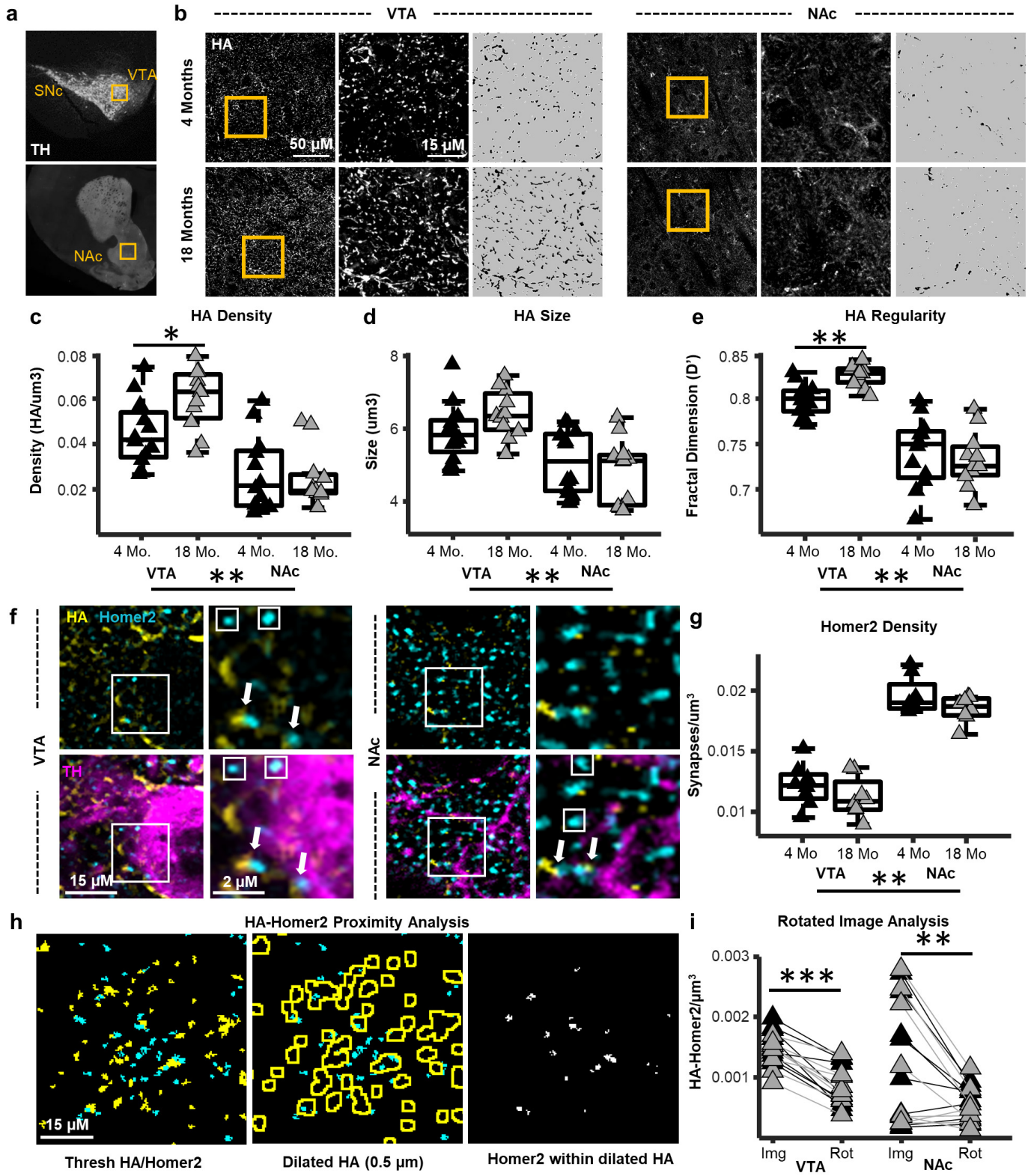
a
SNc
VTA
TH
NAc
b
VTA
NAc
HA
4 Months
18 Months
50 µM
15 µM
c
HA Density
Density (HA/um3)
0.08
0.06
0.04
0.02
*
4 Mo.
18 Mo.
4 Mo.
18 Mo.
VTA
**
NAc
d
HA Size
Size (um3)
8
6
4
4 Mo.
18 Mo.
4 Mo.
18 Mo.
VTA
**
NAc
e
HA Regularity
Fractal Dimension (D')
0.85
0.8
0.75
0.7
**
4 Mo
18 Mo
4 Mo
18 Mo
VTA
**
NAc
f
HA Homer2
TH
VTA
NAc
15 µM
2 µM
g
Homer2 Density
Synapses/um³
0.02
0.015
0.01
4 Mo
18 Mo
4 Mo
18 Mo
VTA
**
NAc
h
HA-Homer2 Proximity Analysis
15 µM
Thresh HA/Homer2
Dilated HA (0.5 µm)
Homer2 within dilated HA
i
Rotated Image Analysis
HA-Homer2/µm³
0.003
0.002
0.001
***
**
Img
Rot
Img
Rot
VTA
NAc

Figure 3

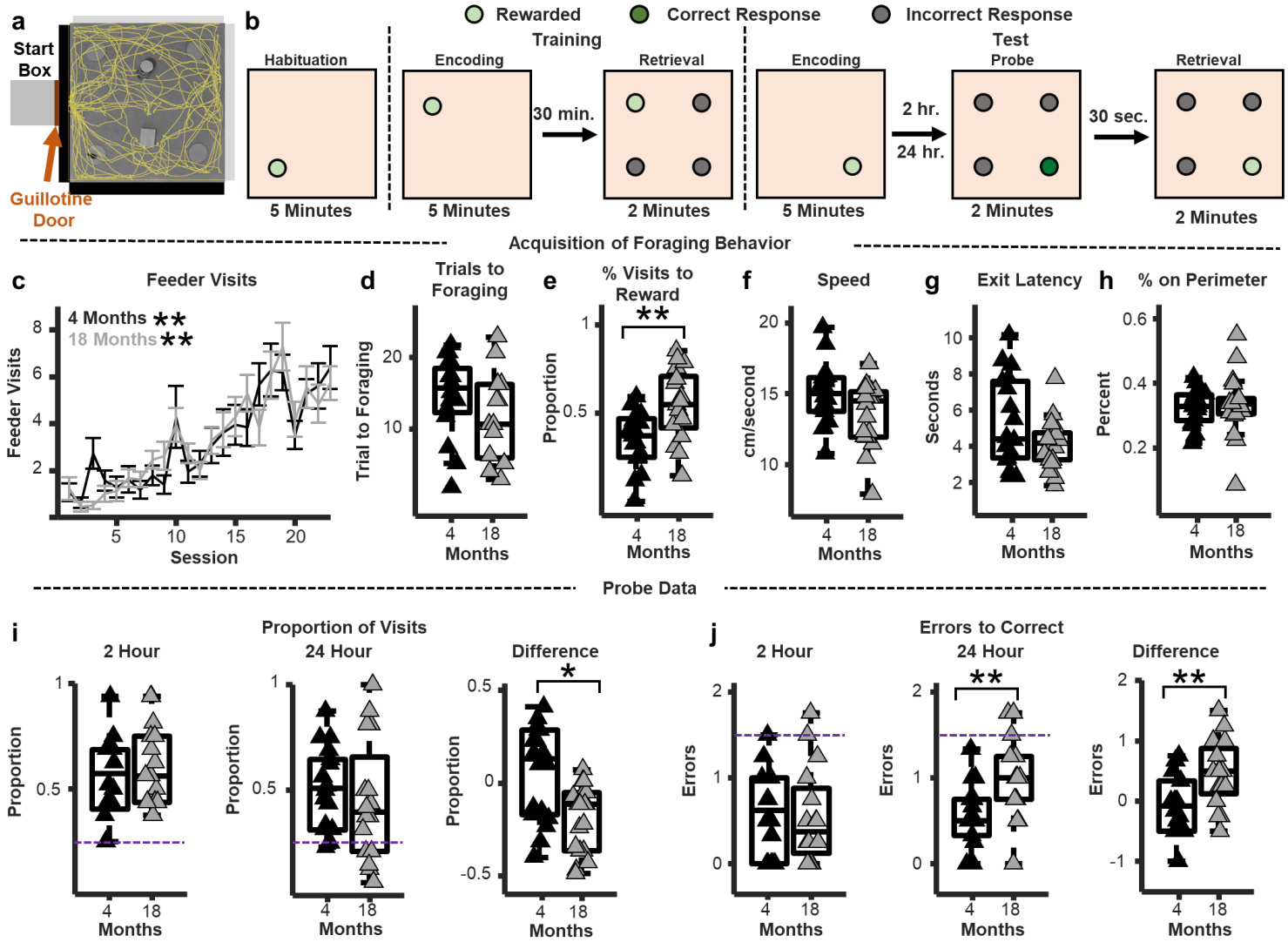
a
Start Box
Guillotine Door
b
Rewarded
Correct Response
Incorrect Response
Training
Test
Habituation
Encoding
Retrieval
Encoding
Probe
Retrieval
30 min.
2 hr.
24 hr.
30 sec.
5 Minutes
5 Minutes
2 Minutes
5 Minutes
2 Minutes
2 Minutes
Acquisition of Foraging Behavior
c
Feeder Visits
4 Months **
18 Months **
Feeder Visits
Session
d
Trials to Foraging
Trial to Foraging
Months
e
% Visits to Reward
**
Proportion
Months
f
Speed
cm/second
Months
g
Exit Latency
Seconds
Months
h
% on Perimeter
Percent
Months
Probe Data
i
Proportion of Visits
2 Hour
24 Hour
Difference
*
Proportion
Months
j
Errors to Correct
2 Hour
24 Hour
Difference
**
**
Errors
Months

Figure 4

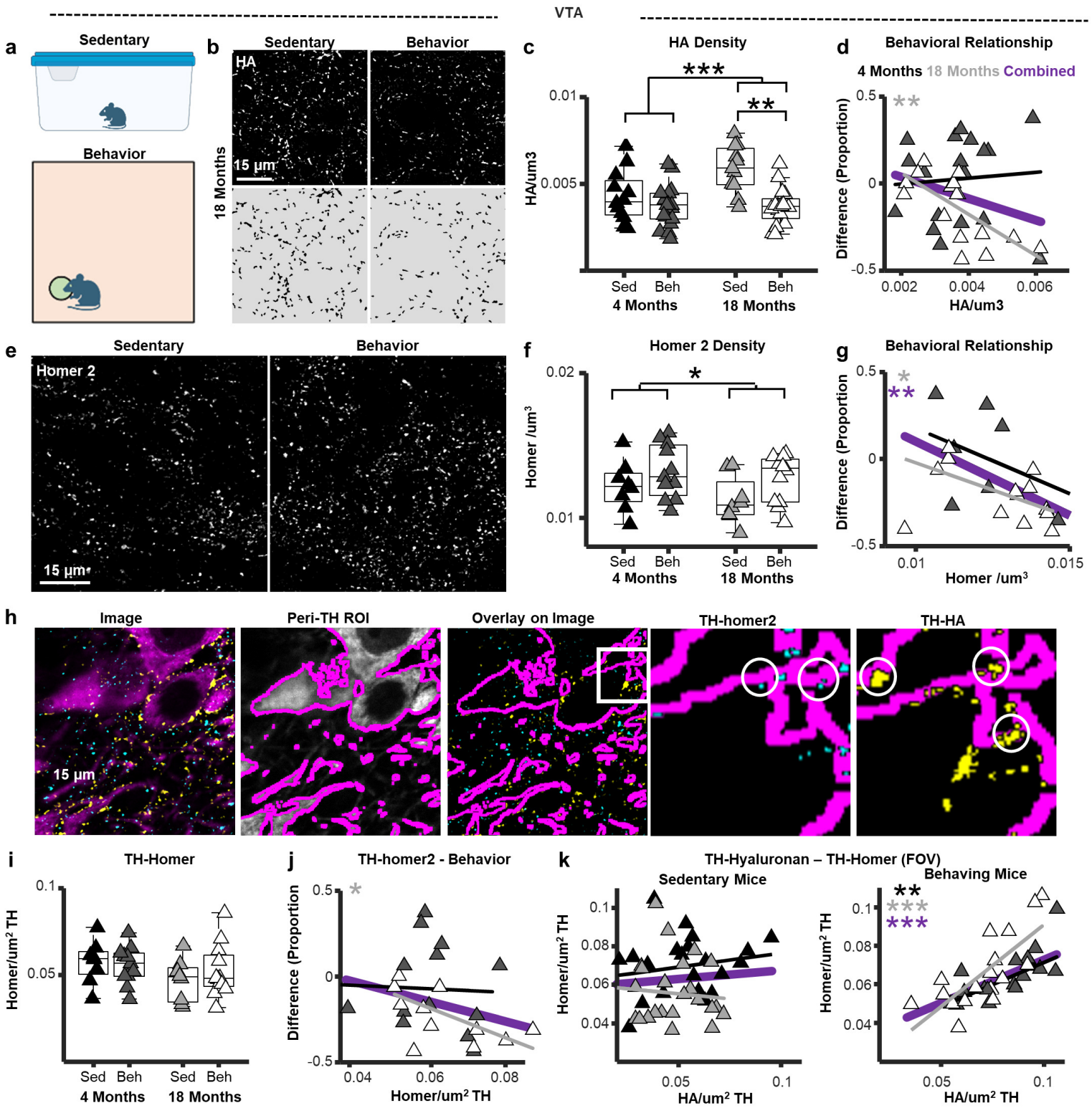
VTA
a
Sedentary
Behavior
b
Sedentary
Behavior
HA
15 µm
18 Months
c
HA Density
***
**
0.01
0.005
HA/um3
Sed
Beh
Sed
Beh
4 Months
18 Months
d
Behavioral Relationship
4 Months 18 Months Combined
**
0.5
0
-0.5
Difference (Proportion)
0.002
0.004
0.006
HA/um3
e
Sedentary
Behavior
Homer 2
15 µm
f
Homer 2 Density
*
0.02
0.01
Homer /um³
Sed
Beh
Sed
Beh
4 Months
18 Months
g
Behavioral Relationship
*
**
0.5
0
-0.5
Difference (Proportion
0.01
0.015
Homer /um³
h
Image
Peri-TH ROI
Overlay on Image
TH-homer2
TH-HA
15 µm
i
TH-Homer
0.1
0.05
Homer/um² TH
Sed
Beh
Sed
Beh
4 Months
18 Months
j
TH-homer2 - Behavior
*
0.5
0
-0.5
Difference (Proportion
0.04
0.06
0.08
Homer/um² TH
k
TH-Hyaluronan – TH-Homer (FOV)
Sedentary Mice
Behaving Mice
**
***
***
0.1
0.08
0.06
0.04
Homer/um² TH
0.05
0.1
HA/um² TH

Figure 5

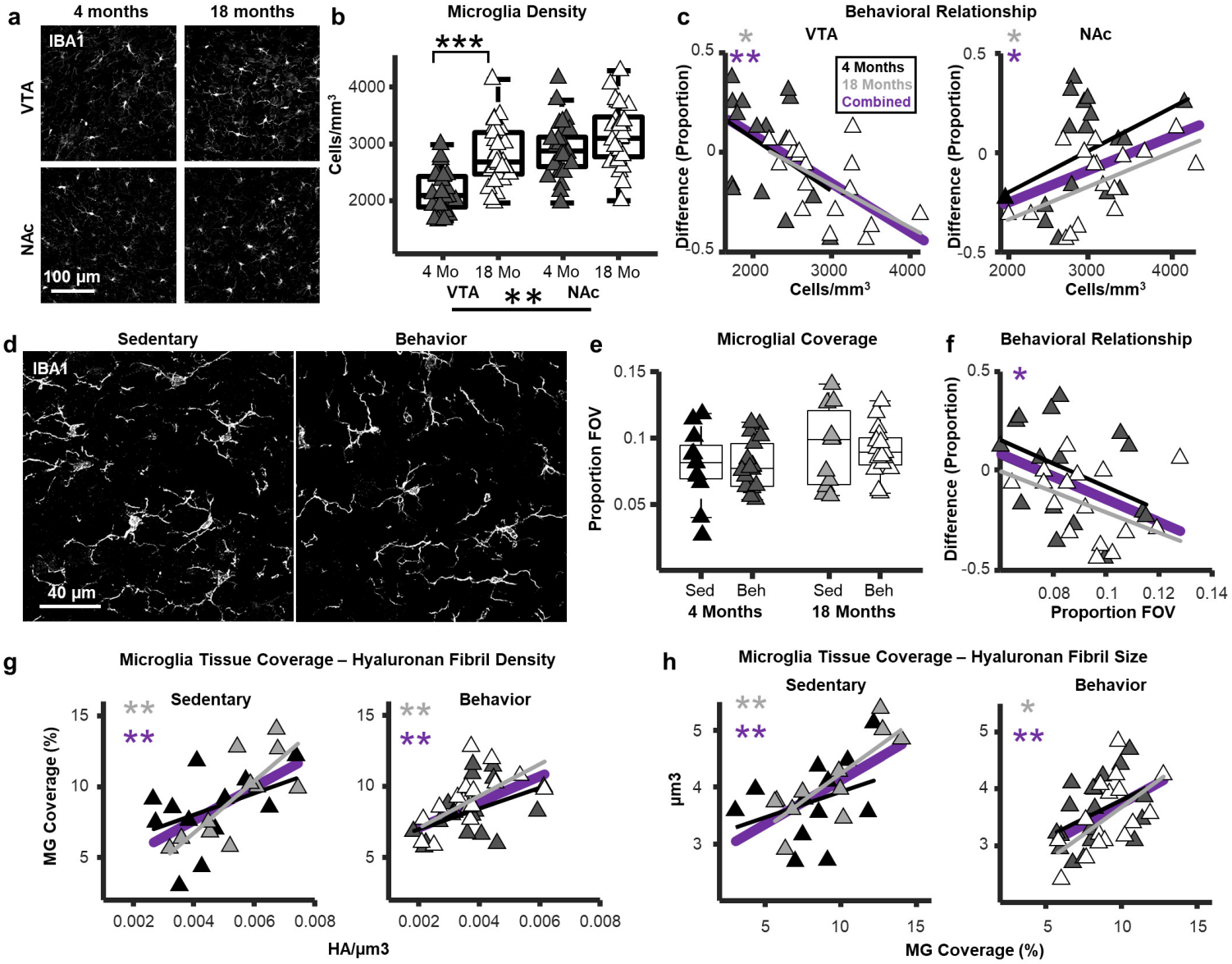
a
4 months
18 months
IBA1
VTA
NAc
100 µm
b
Microglia Density
***
Cells/mm³
4000
3000
2000
4 Mo
18 Mo
4 Mo
18 Mo
VTA
**
NAc
c
Behavioral Relationship
VTA
NAc
4 Months
18 Months
Combined
Difference (Proportion)
0.5
0
-0.5
2000
3000
4000
Cells/mm³
d
Sedentary
Behavior
IBA1
40 µm
e
Microglial Coverage
Proportion FOV
0.15
0.1
0.05
Sed
Beh
Sed
Beh
4 Months
18 Months
f
Behavioral Relationship
Difference (Proportion)
0.5
0
-0.5
0.08
0.1
0.12
0.14
Proportion FOV
g
Microglia Tissue Coverage – Hyaluronan Fibril Density
Sedentary
Behavior
MG Coverage (%)
15
10
5
0.002
0.004
0.006
0.008
HA/µm3
h
Microglia Tissue Coverage – Hyaluronan Fibril Size
Sedentary
Behavior
µm3
5
4
3
5
10
15
MG Coverage (%)

Figure 6

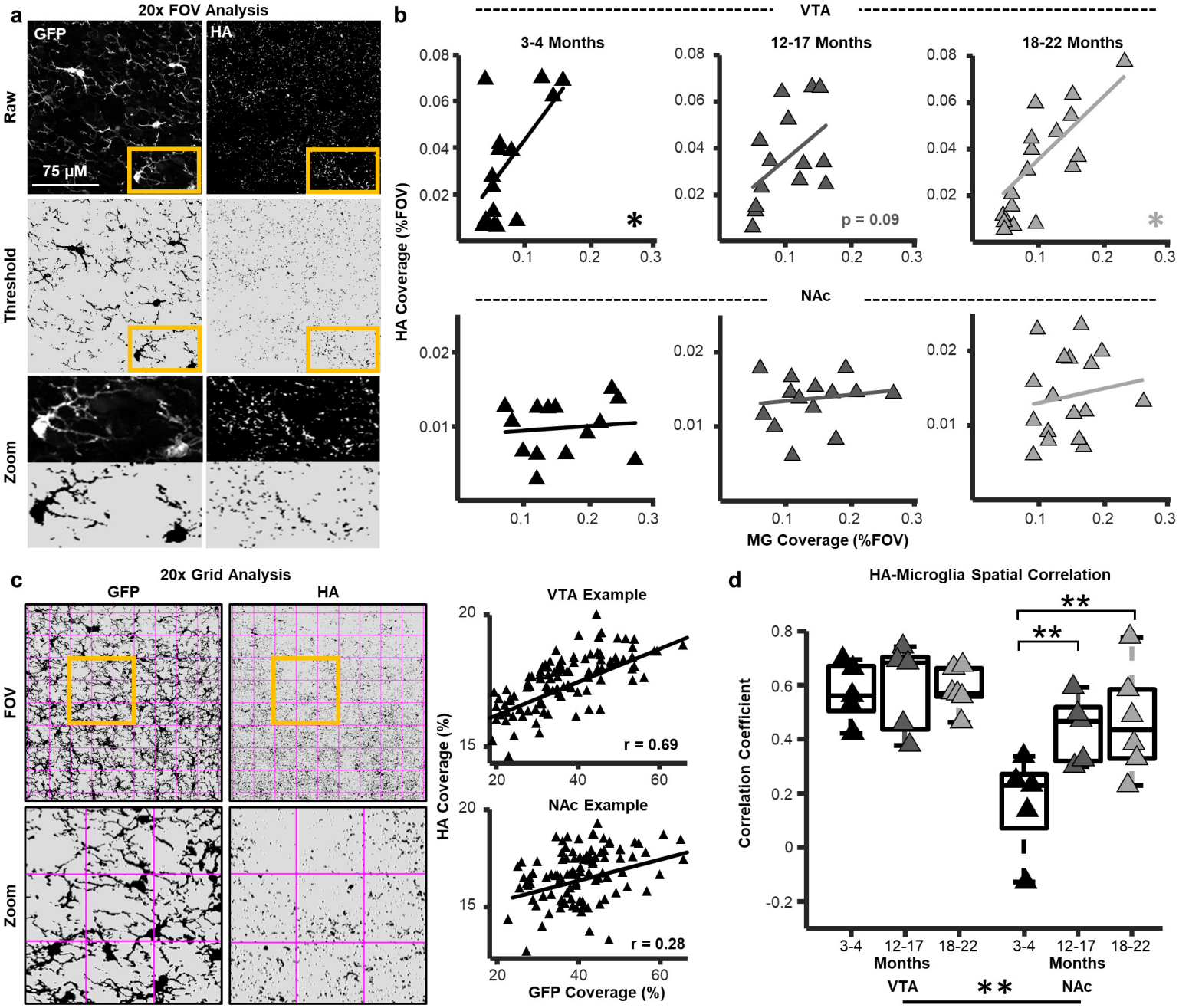
a
20x FOV Analysis
GFP
HA
Raw
75 µM
Threshold
Zoom
b
VTA
3-4 Months
12-17 Months
18-22 Months
HA Coverage (%FOV)
p = 0.09
NAc
MG Coverage (%FOV)
c
20x Grid Analysis
GFP
HA
FOV
Zoom
VTA Example
r = 0.69
NAc Example
r = 0.28
HA Coverage (%)
GFP Coverage (%)
d
HA-Microglia Spatial Correlation
Correlation Coefficient
3-4
12-17
18-22
Months
VTA
NAc

Figure 7

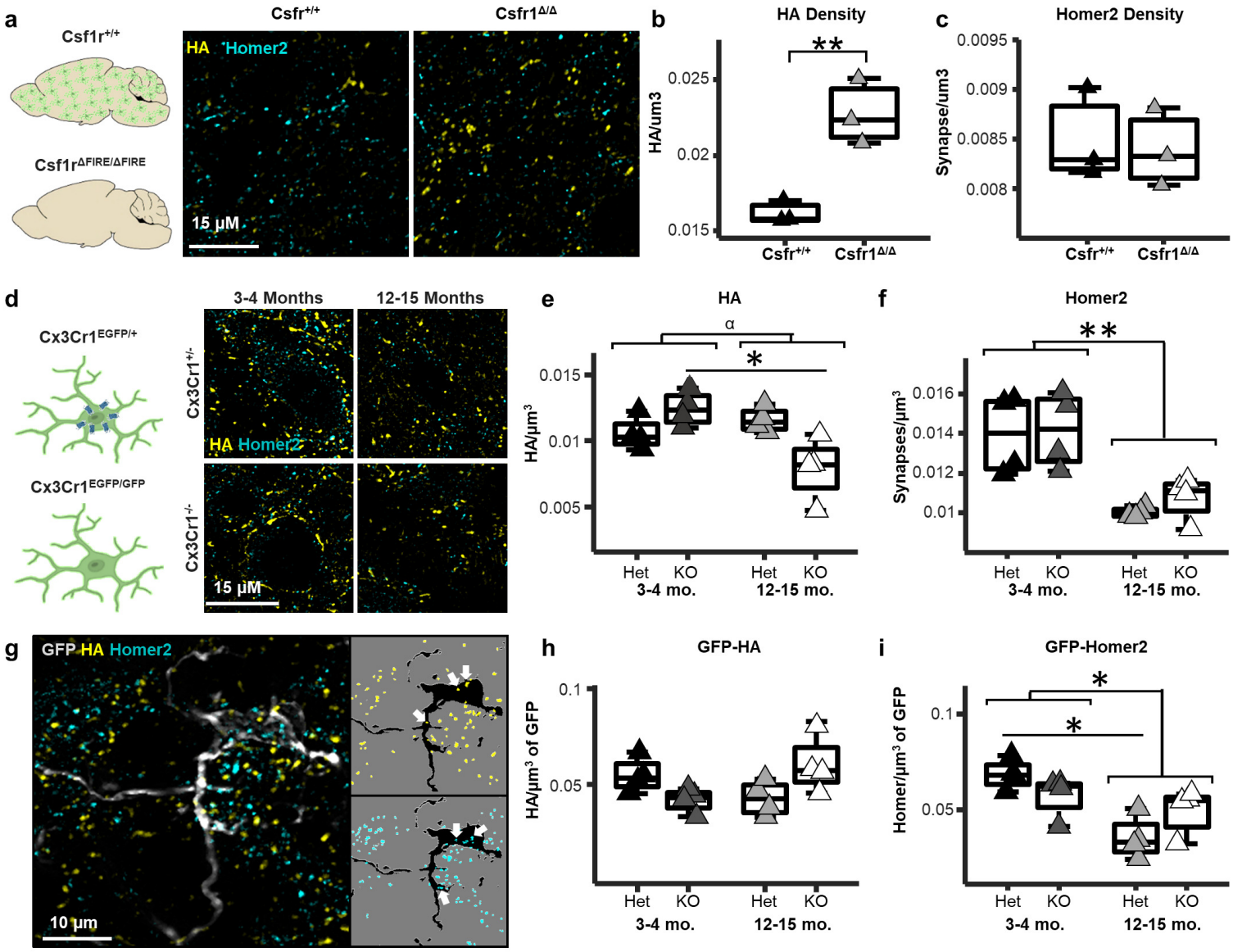
a
Csf1r+/+
Csf1rΔFIRE/ΔFIRE
Csfr+/+
Csfr1Δ/Δ
HA Homer2
15 µM
b
HA Density
HA/um3
0.025
0.02
0.015
**
Csfr+/+
Csfr1Δ/Δ
c
Homer2 Density
Synapse/um3
0.0095
0.009
0.0085
0.008
Csfr+/+
Csfr1Δ/Δ
d
Cx3Cr1EGFP/+
Cx3Cr1EGFP/GFP
3-4 Months
12-15 Months
Cx3Cr1+/-
Cx3Cr1-/-
HA Homer2
15 µM
e
HA
HA/µm3
0.015
0.01
0.005
α
*
Het
KO
Het
KO
3-4 mo.
12-15 mo.
f
Homer2
Synapses/µm3
0.016
0.014
0.012
0.01
**
Het
KO
Het
KO
3-4 mo.
12-15 mo.
g
GFP HA Homer2
10 µm
h
GFP-HA
HA/µm3 of GFP
0.1
0.05
Het
KO
Het
KO
3-4 mo.
12-15 mo.
i
GFP-Homer2
Homer/µm3 of GFP
0.1
0.05
*
*
Het
KO
Het
KO
3-4 mo.
12-15 mo.

Figure 8

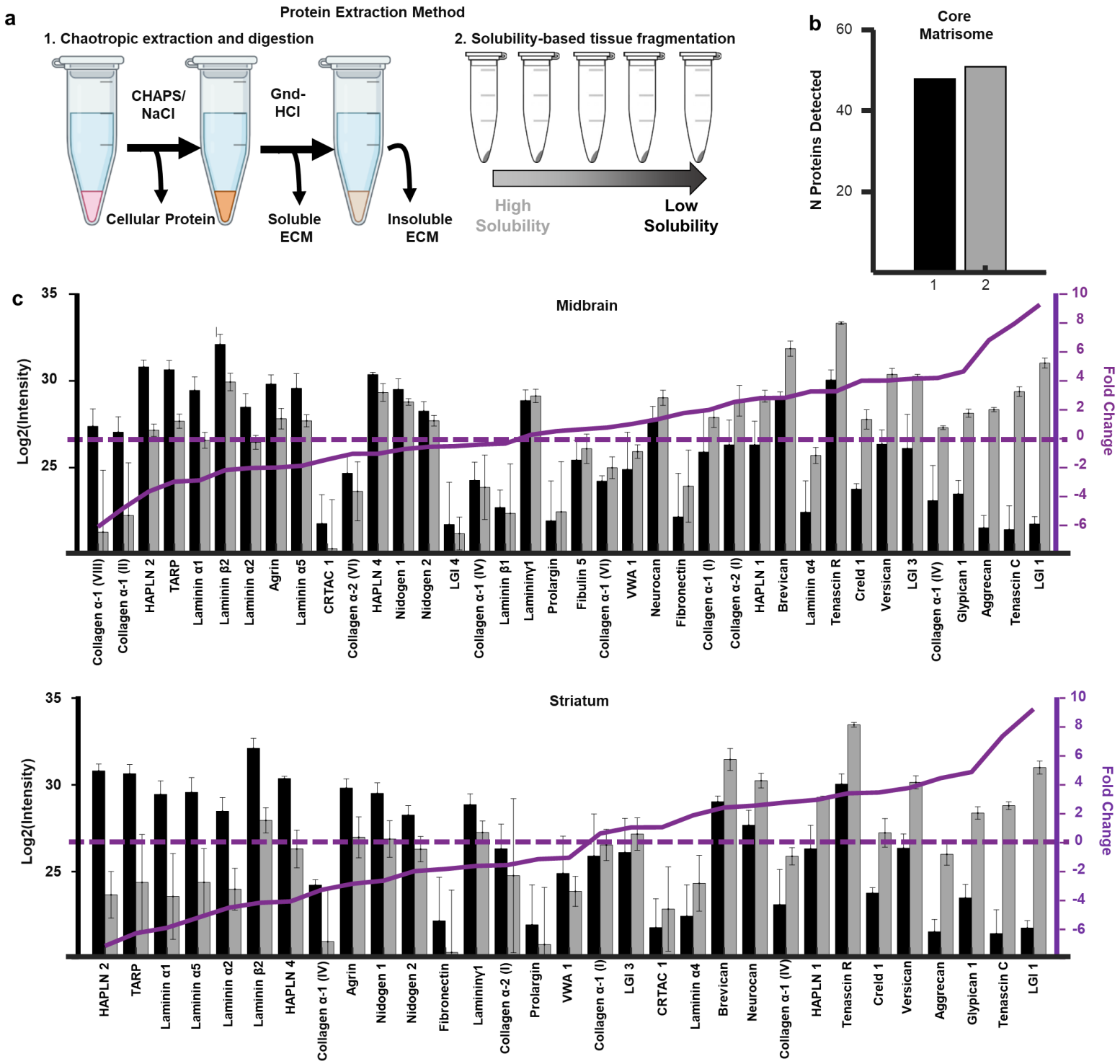

Ext. Data Fig. 1

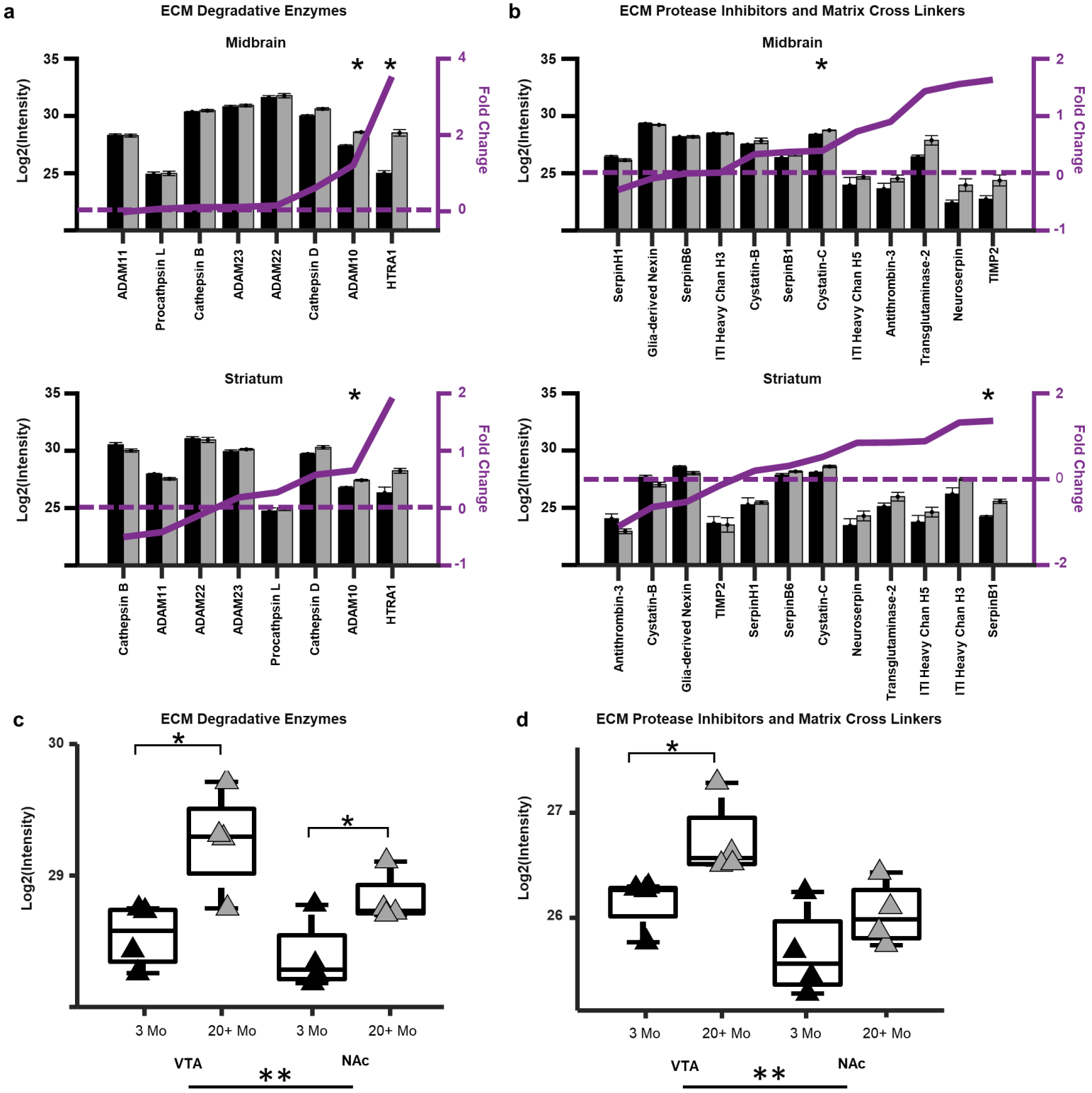

Ext. Data Fig. 2

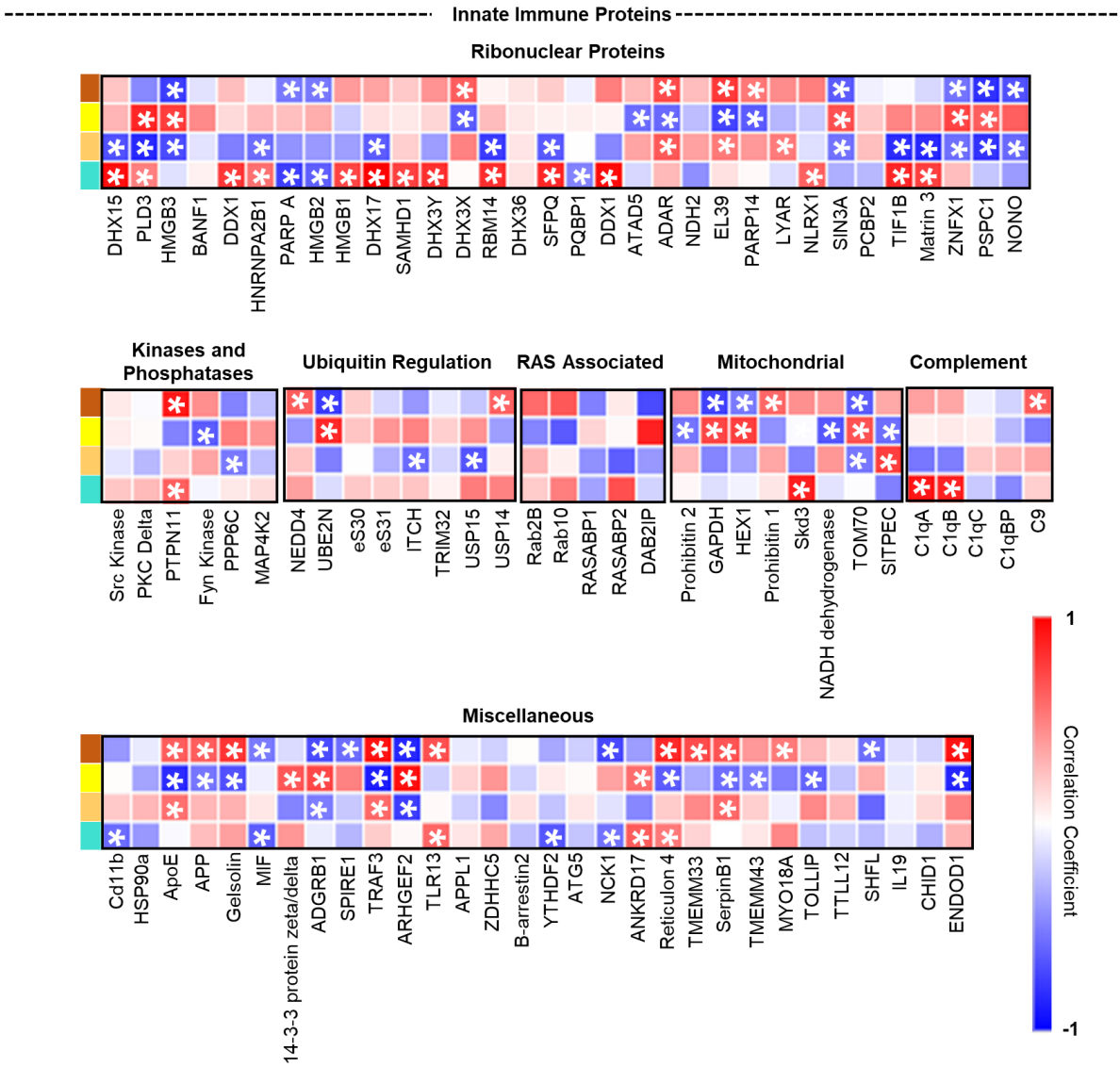

Ext. Data Fig. 3

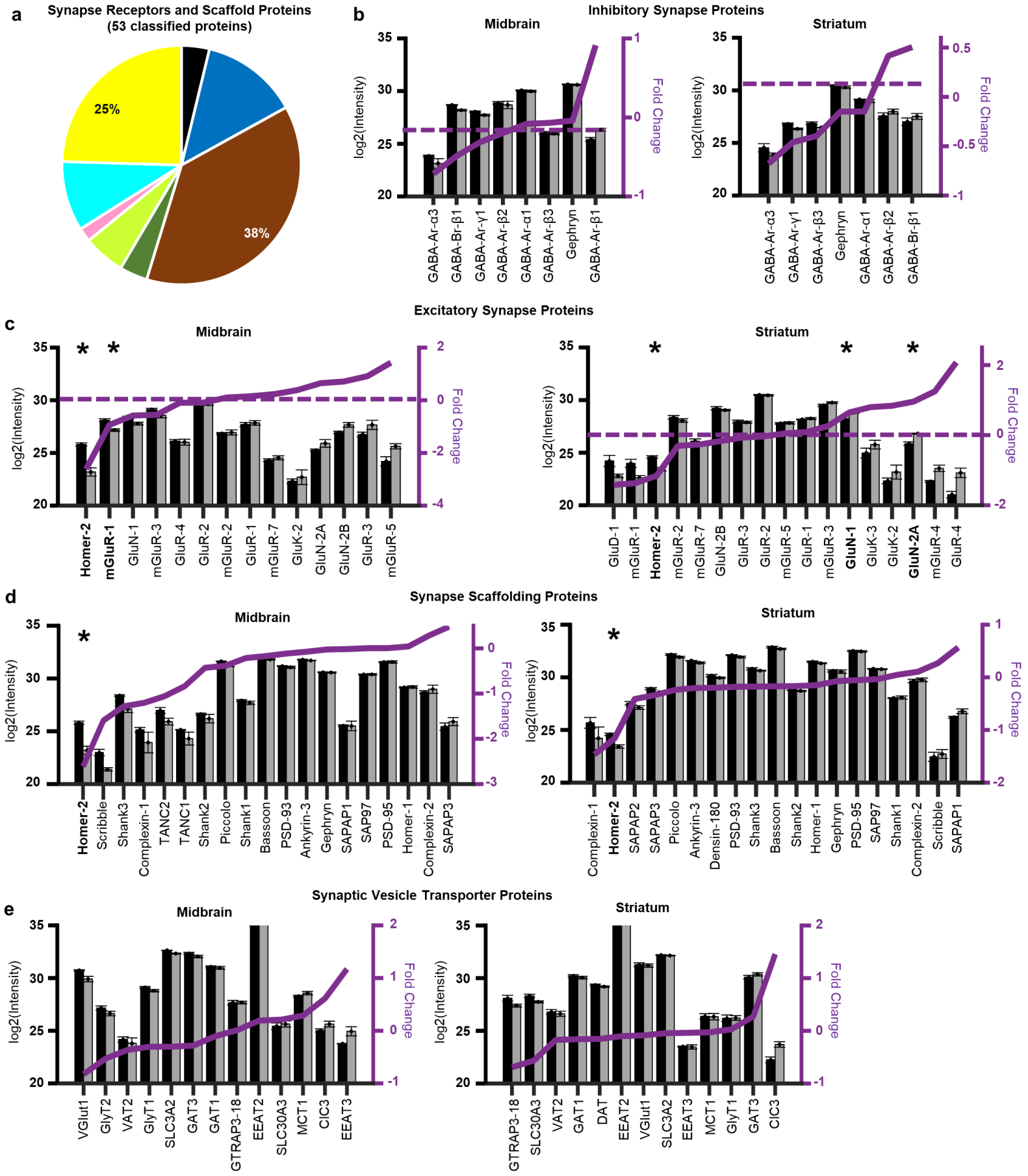

Ext. Data Fig. 4

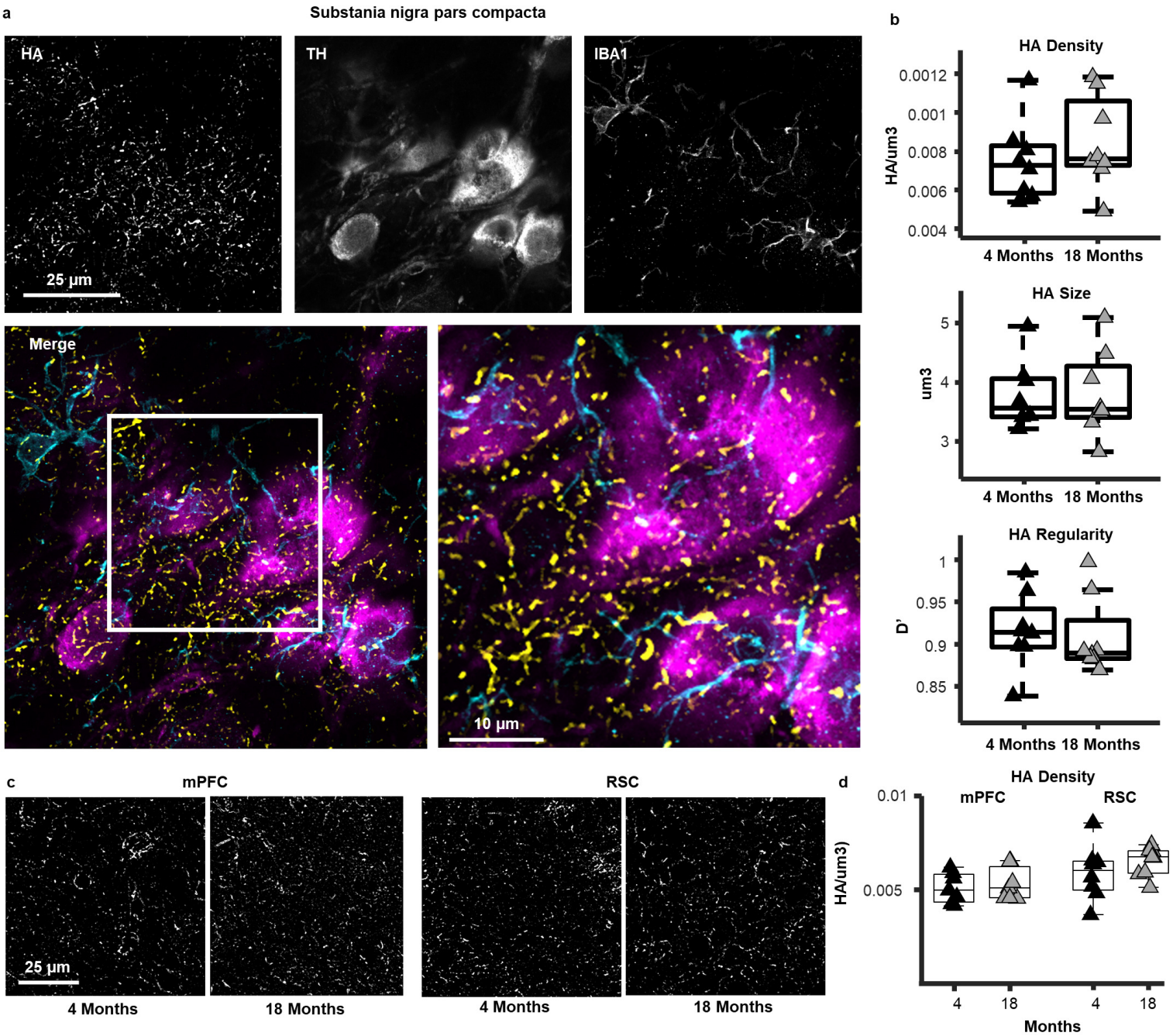

Ext. Data Fig. 5

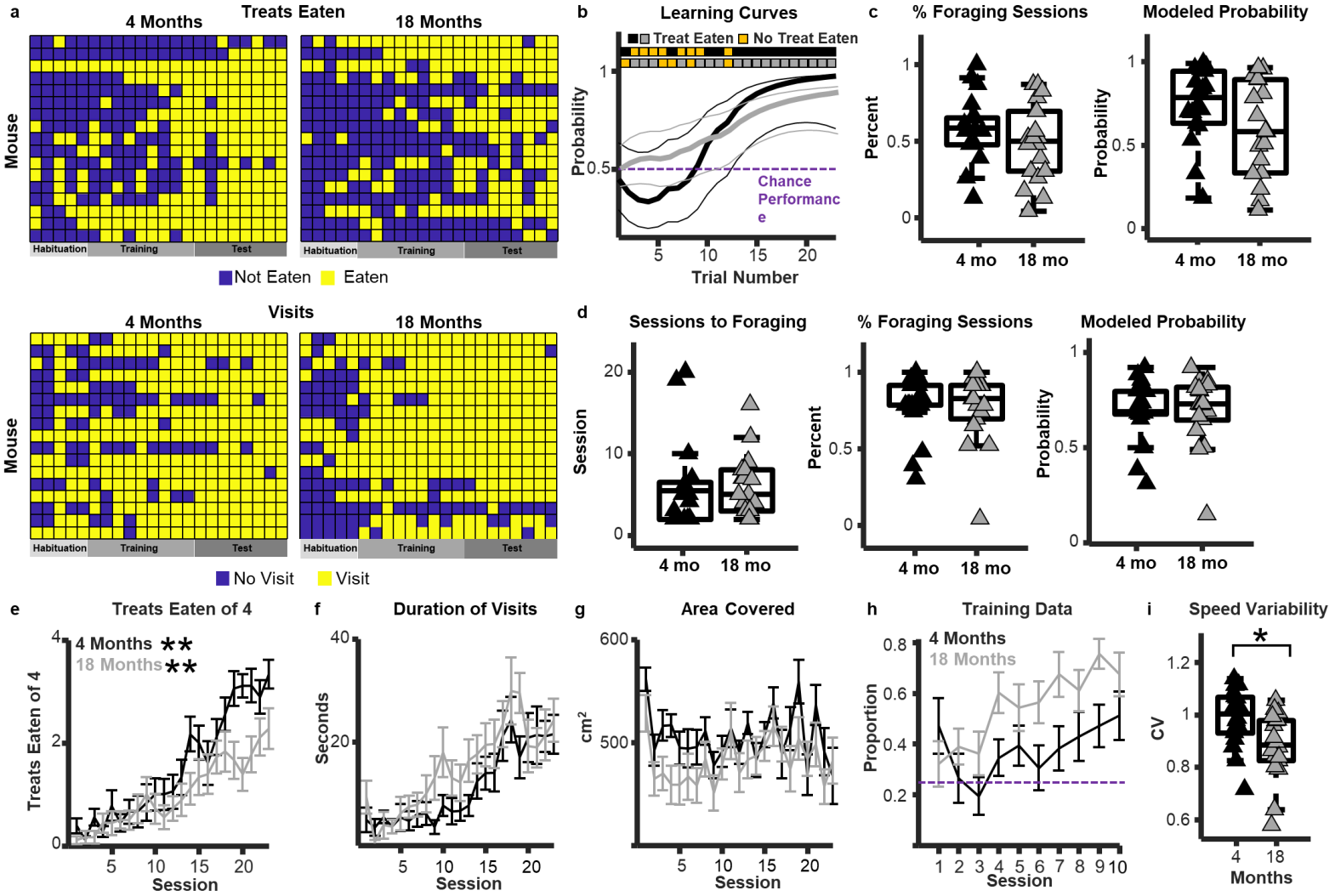

f

Ext. Data Fig. 6

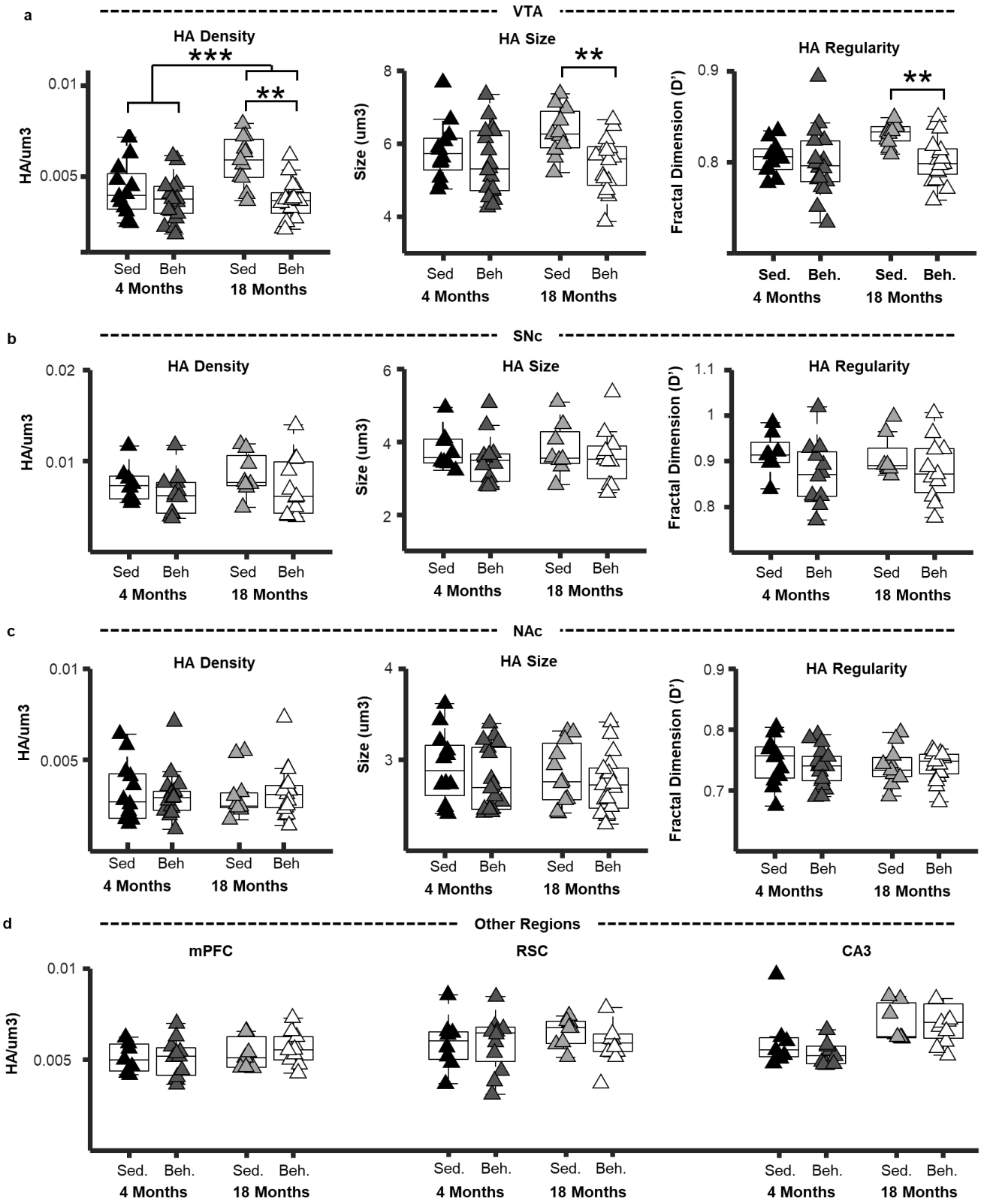

Ext. Data Fig. 7

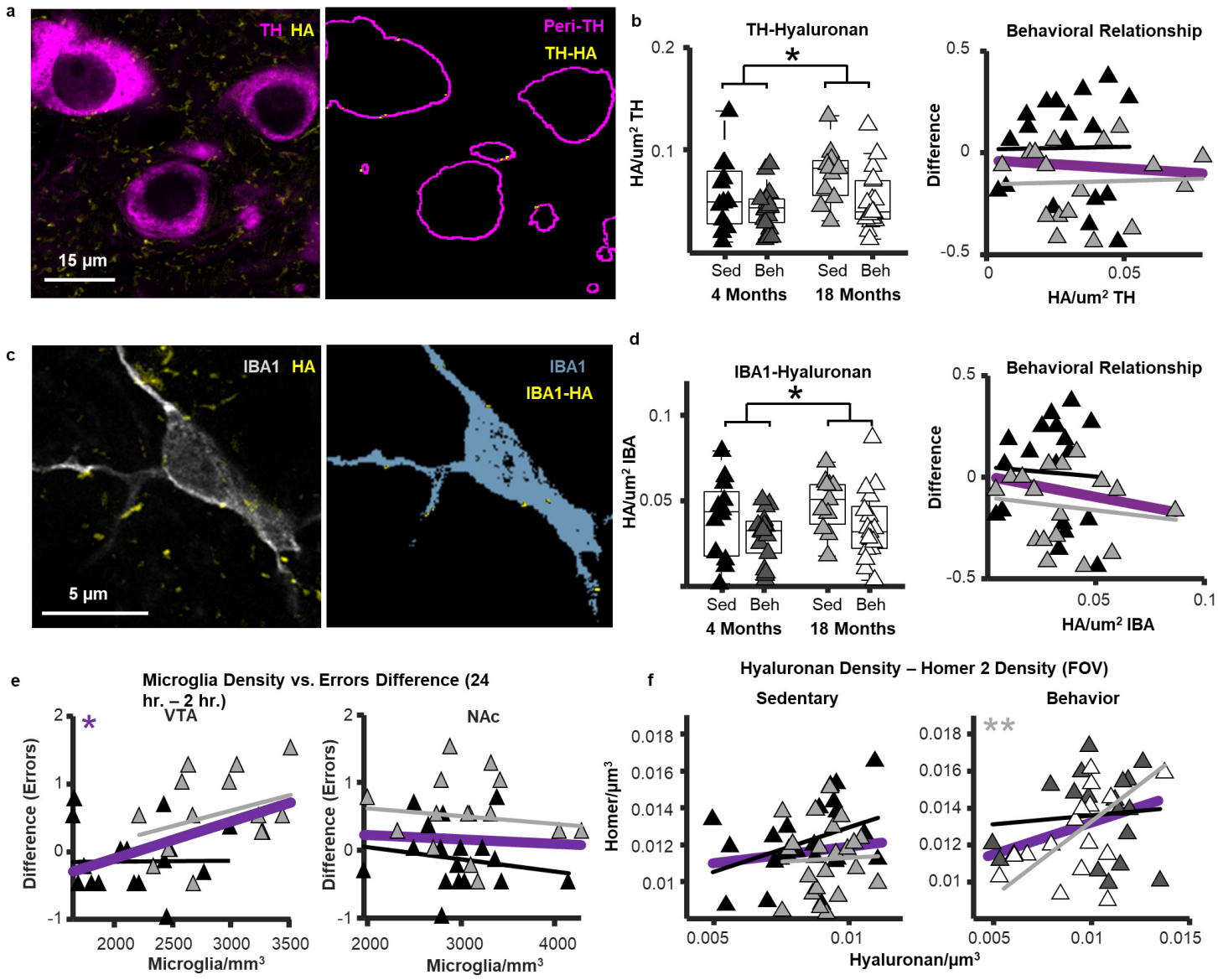

Ext. Data Fig. 8

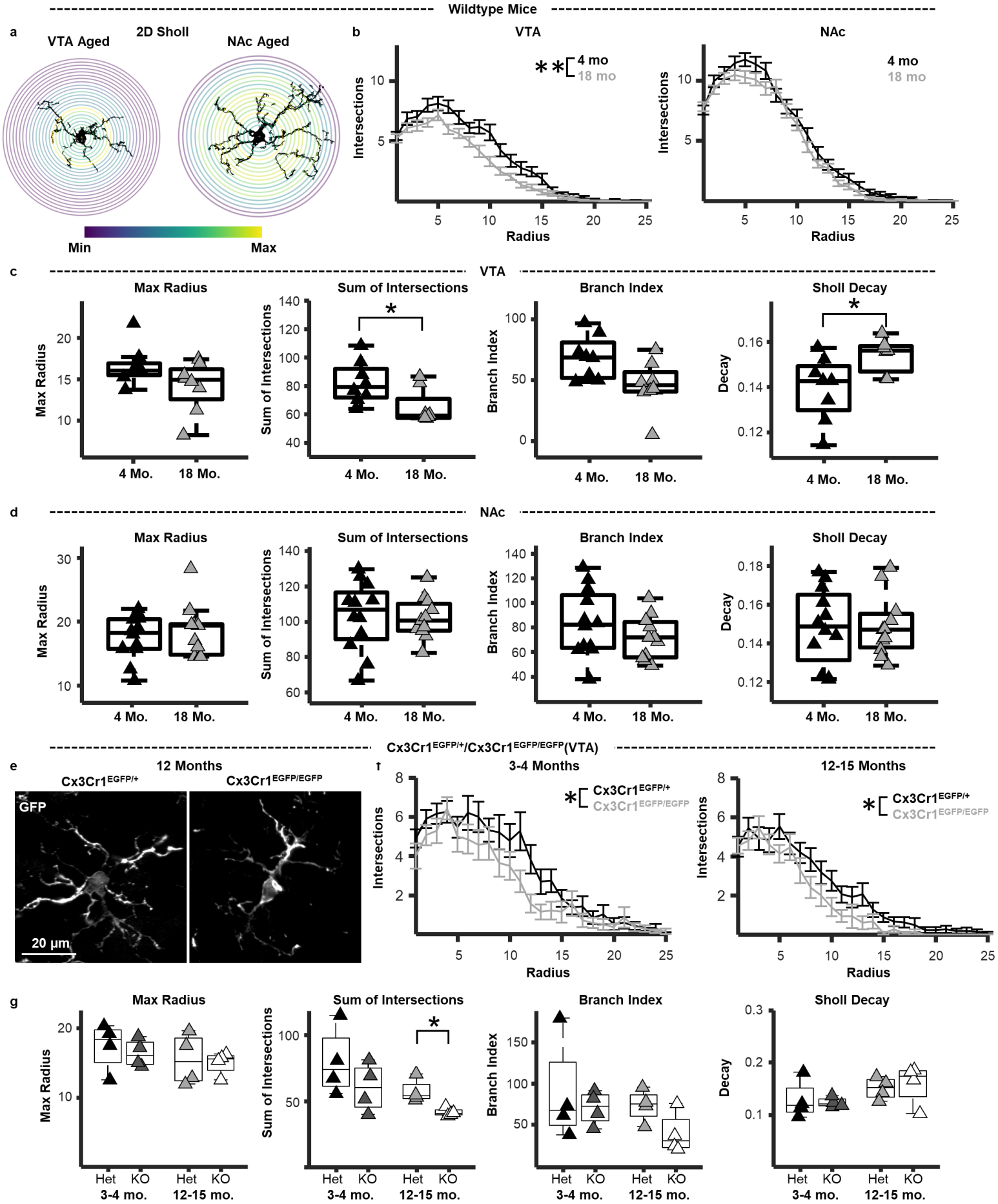

Ext. Data Fig. 9

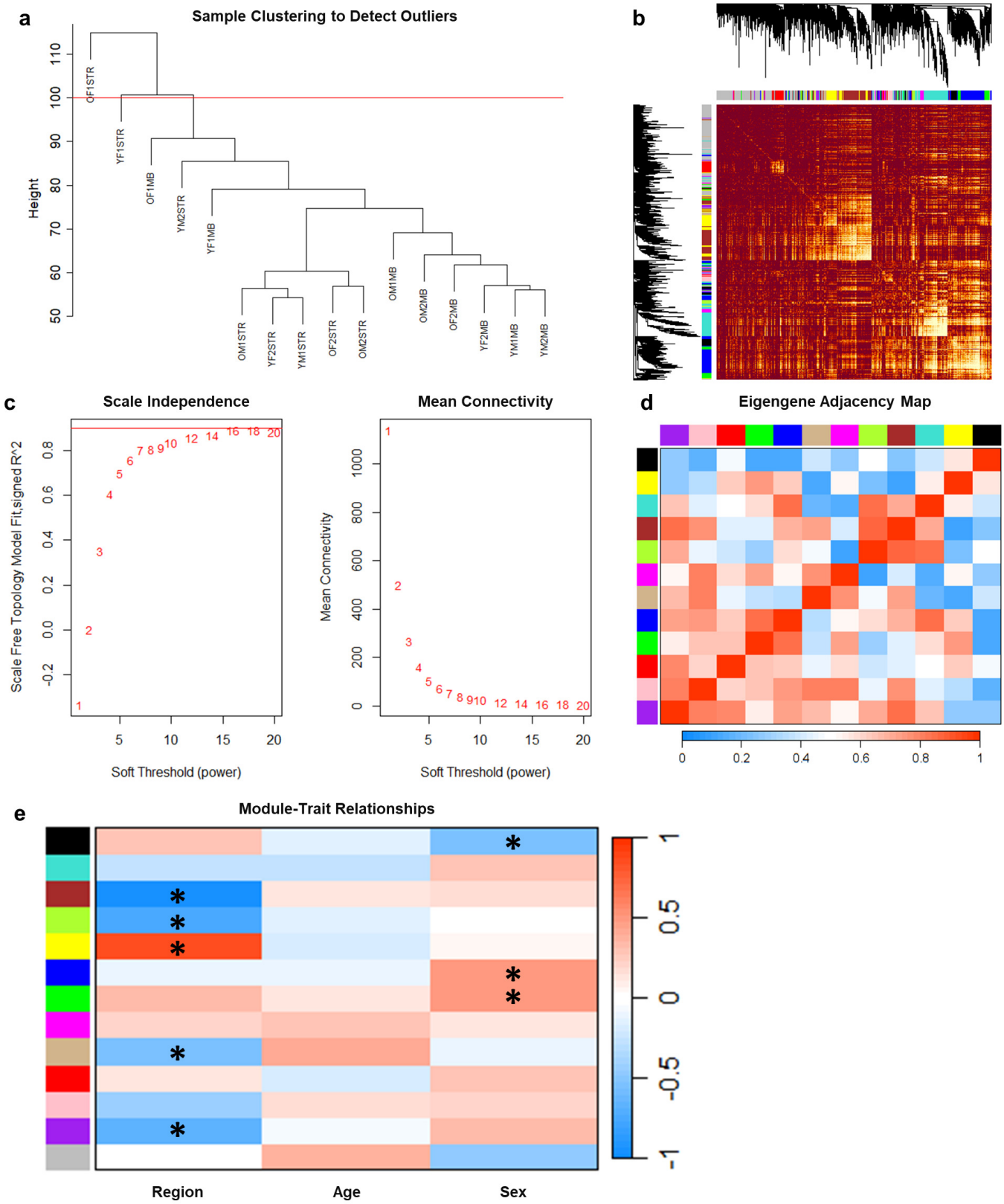
a
Sample Clustering to Detect Outliers
Height
OF1STR
YF1STR
OF1MB
YM2STR
YF1MB
OM1STR
YF2STR
YM1STR
OF2STR
OM2STR
OM1MB
OM2MB
OF2MB
YF2MB
YM1MB
YM2MB
b
c
Scale Independence
Scale Free Topology Model Fit,signed R^2
Soft Threshold (power)
Mean Connectivity
Mean Connectivity
Soft Threshold (power)
d
Eigengene Adjacency Map
e
Module-Trait Relationships
Region
Age
Sex

Figure S1

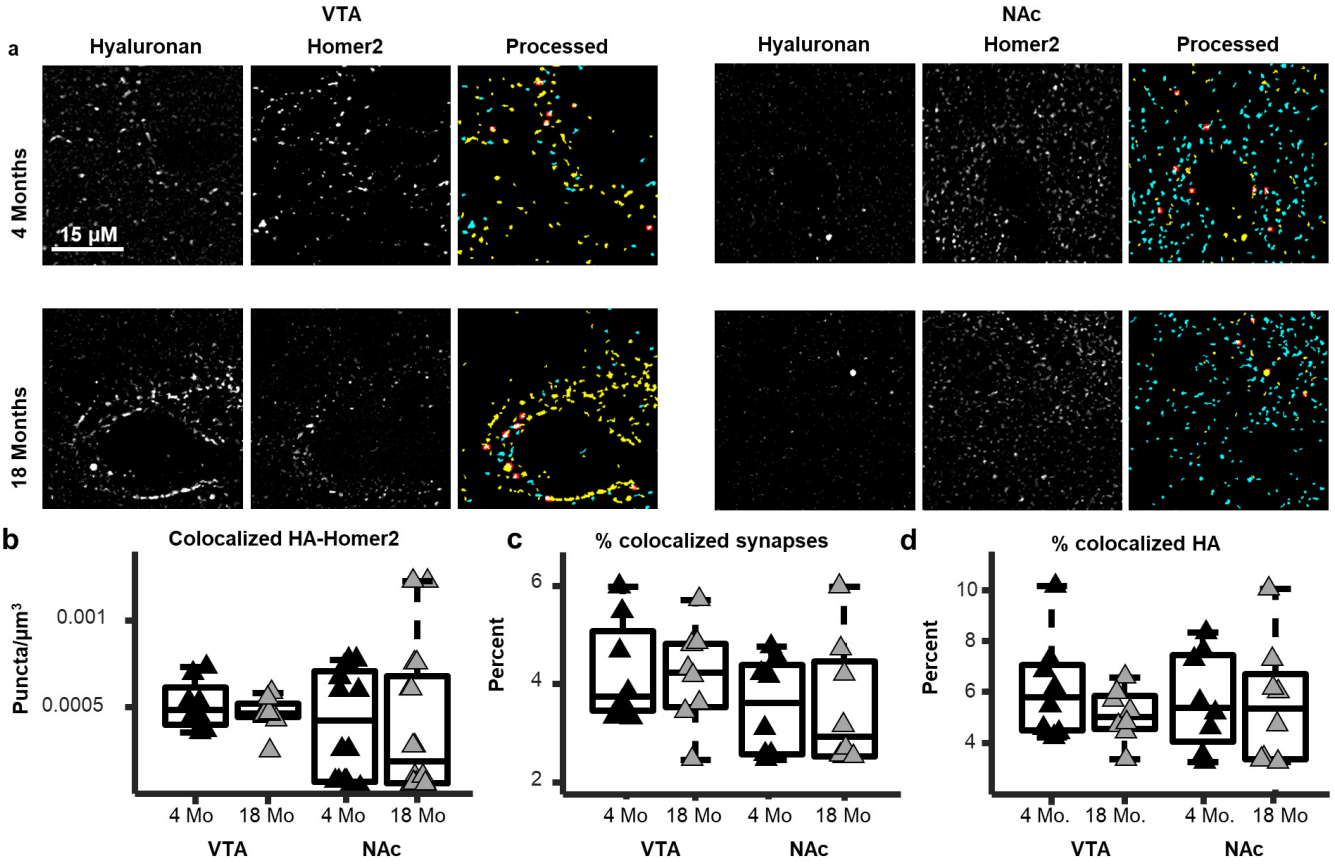
a
VTA
NAc
Hyaluronan
Homer2
Processed
Hyaluronan
Homer2
Processed
4 Months
15 µM
18 Months
b
Colocalized HA-Homer2
Puncta/µm³
0.001
0.0005
4 Mo
18 Mo
4 Mo
18 Mo
VTA
NAc
c
% colocalized synapses
Percent
6
4
2
4 Mo
18 Mo
4 Mo
18 Mo
VTA
NAc
d
% colocalized HA
Percent
10
8
6
4
4 Mo.
18 Mo.
4 Mo.
18 Mo
VTA
NAc

Figure S2

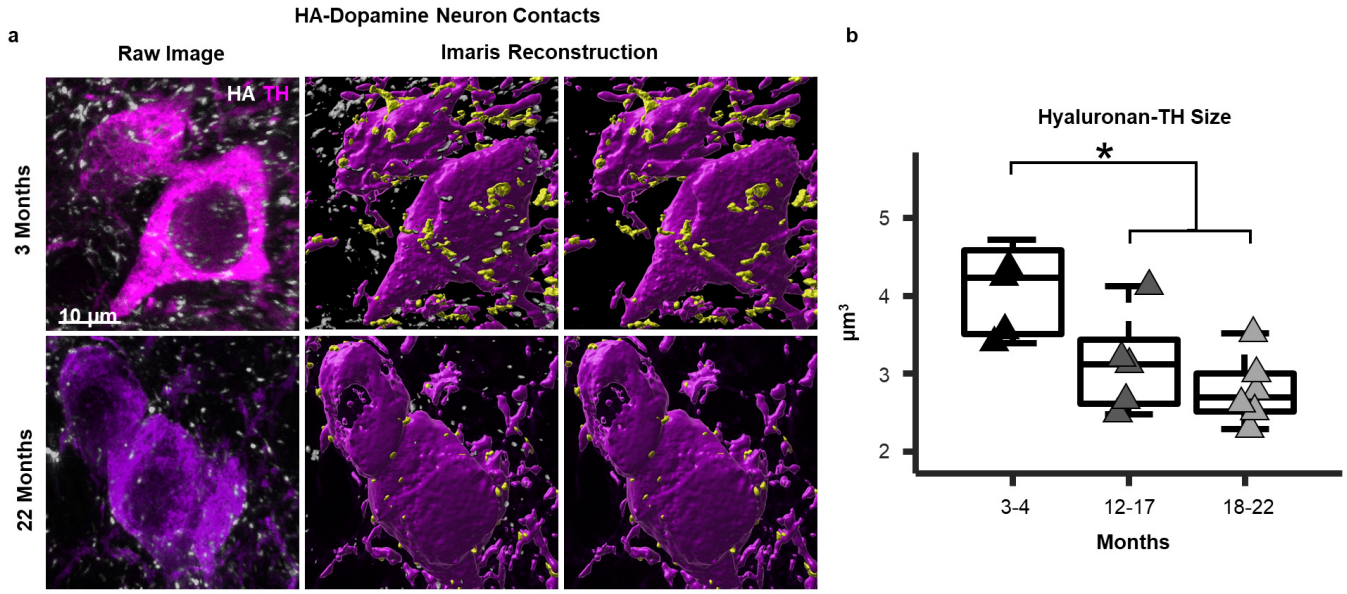
a
HA-Dopamine Neuron Contacts
Raw Image
Imaris Reconstruction
HA TH
10 µm
3 Months
22 Months
b
Hyaluronan-TH Size
*
µm³
5
4
3
2
3-4
12-17
18-22
Months

Figure S3

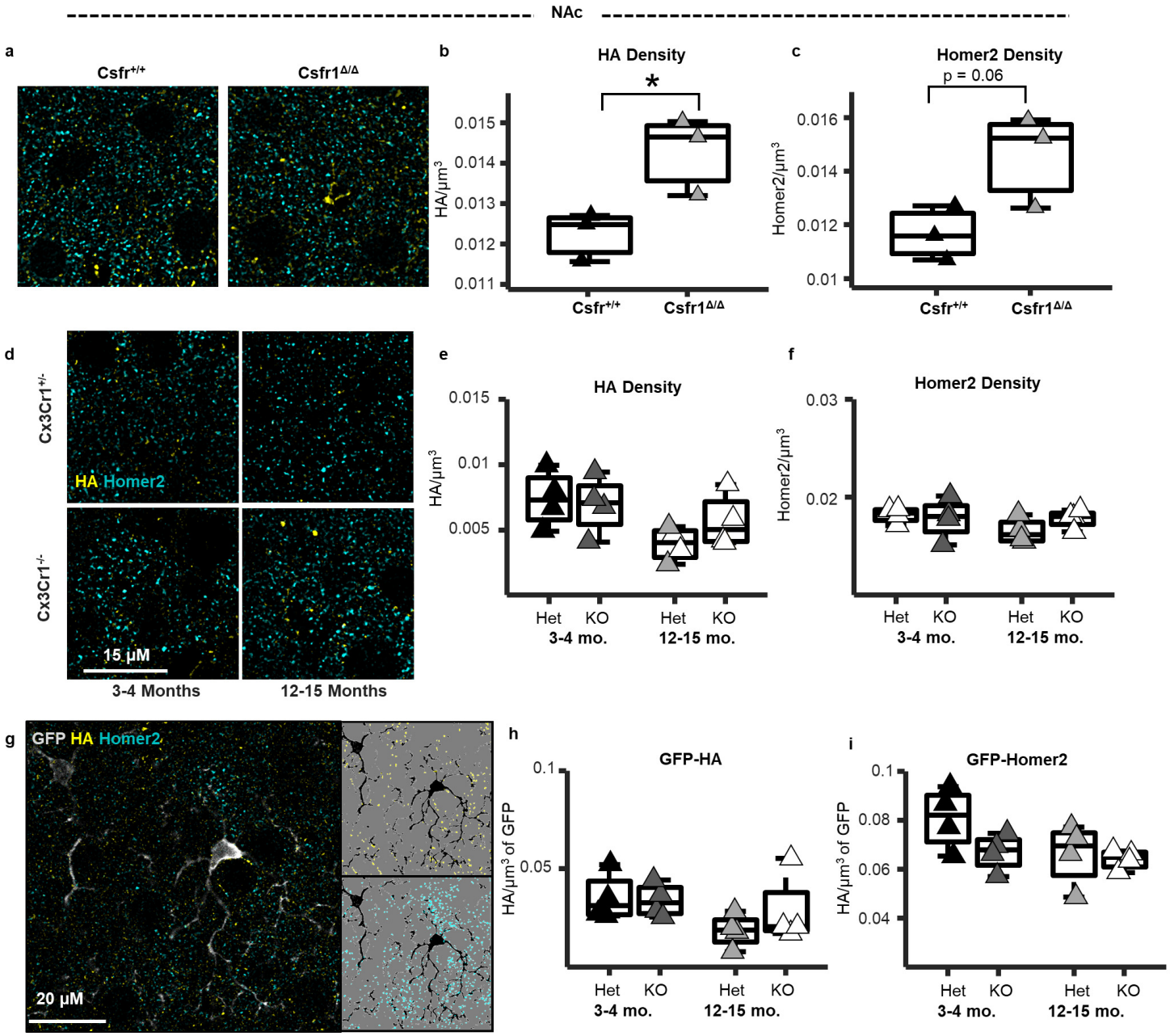
NAc
a
Csfr+/+
Csfr1Δ/Δ
b
HA Density
*
HA/µm3
0.015
0.014
0.013
0.012
0.011
Csfr+/+
Csfr1Δ/Δ
c
Homer2 Density
p = 0.06
Homer2/µm3
0.016
0.014
0.012
0.01
Csfr+/+
Csfr1Δ/Δ
d
Cx3Cr1+/-
Cx3Cr1-/-
HA Homer2
15 µM
3-4 Months
12-15 Months
e
HA Density
HA/µm3
0.015
0.01
0.005
Het
KO
Het
KO
3-4 mo.
12-15 mo.
f
Homer2 Density
Homer2/µm3
0.03
0.02
Het
KO
Het
KO
3-4 mo.
12-15 mo.
g
GFP HA Homer2
20 µM
h
GFP-HA
HA/µm3 of GFP
0.1
0.05
Het
KO
Het
KO
3-4 mo.
12-15 mo.
i
GFP-Homer2
HA/µm3 of GFP
0.1
0.08
0.06
0.04
Het
KO
Het
KO
3-4 mo.
12-15 mo.

Figure S4

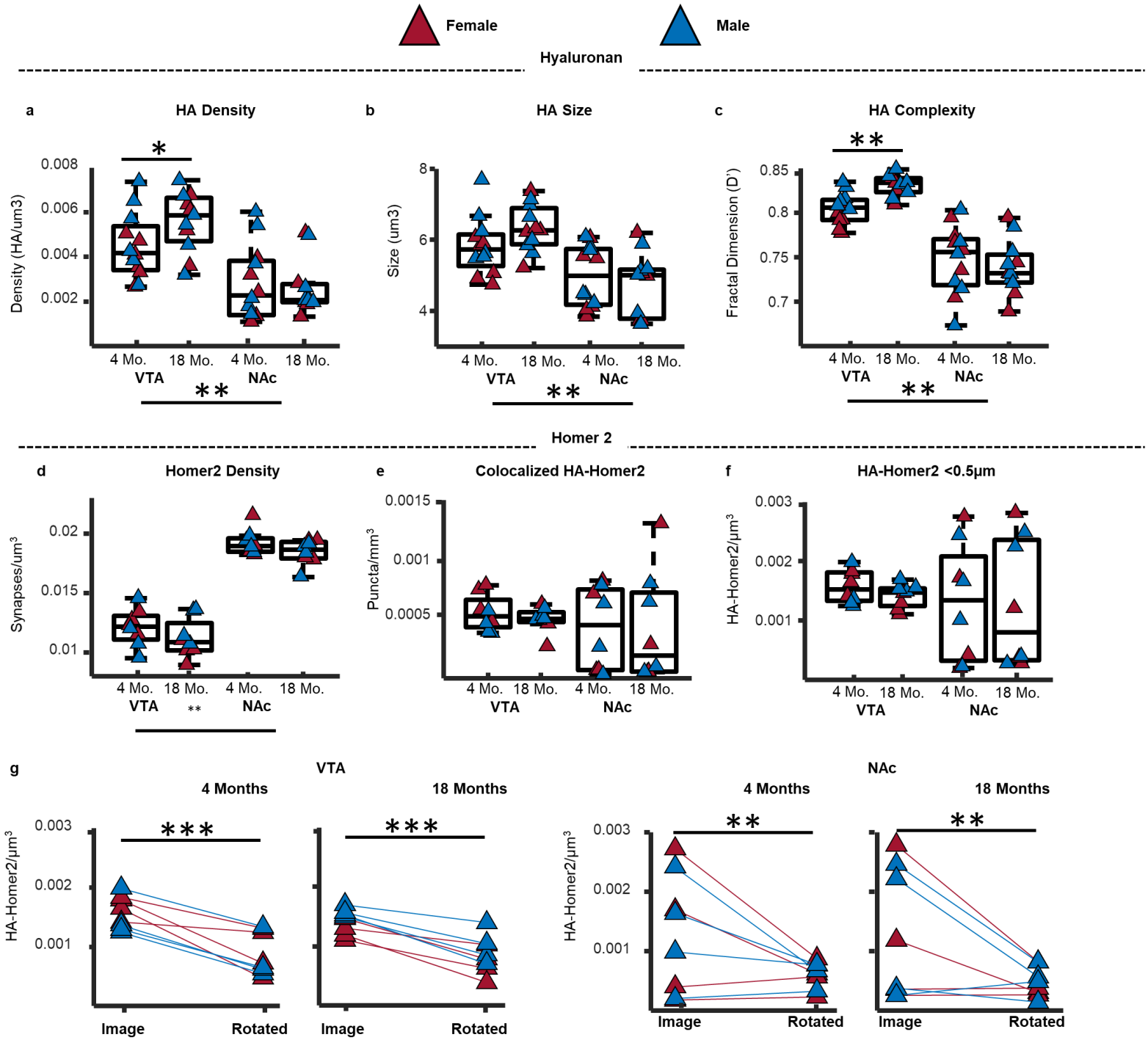
Female
Male
Hyaluronan
a
HA Density
Density (HA/um3)
0.008
0.006
0.004
0.002
*
4 Mo.
18 Mo.
4 Mo.
18 Mo.
VTA
NAc
**
b
HA Size
Size (um3)
8
6
4
4 Mo.
18 Mo.
4 Mo.
18 Mo.
VTA
NAc
**
c
HA Complexity
Fractal Dimension (D')
0.85
0.8
0.75
0.7
**
4 Mo.
18 Mo.
4 Mo.
18 Mo.
VTA
NAc
**
Homer 2
d
Homer2 Density
Synapses/um³
0.02
0.015
0.01
4 Mo.
18 Mo.
4 Mo.
18 Mo.
VTA
**
NAc
e
Colocalized HA-Homer2
Puncta/mm³
0.0015
0.001
0.0005
4 Mo.
18 Mo.
4 Mo.
18 Mo.
VTA
NAc
f
HA-Homer2 <0.5µm
HA-Homer2/µm³
0.003
0.002
0.001
4 Mo.
18 Mo.
4 Mo.
18 Mo.
VTA
NAc
g
VTA
4 Months
18 Months
HA-Homer2/µm³
0.003
0.002
0.001
***
***
Image
Rotated
Image
Rotated
NAc
4 Months
18 Months
HA-Homer2/µm³
0.003
0.002
0.001
**
**
Image
Rotated
Image
Rotated

Figure S5

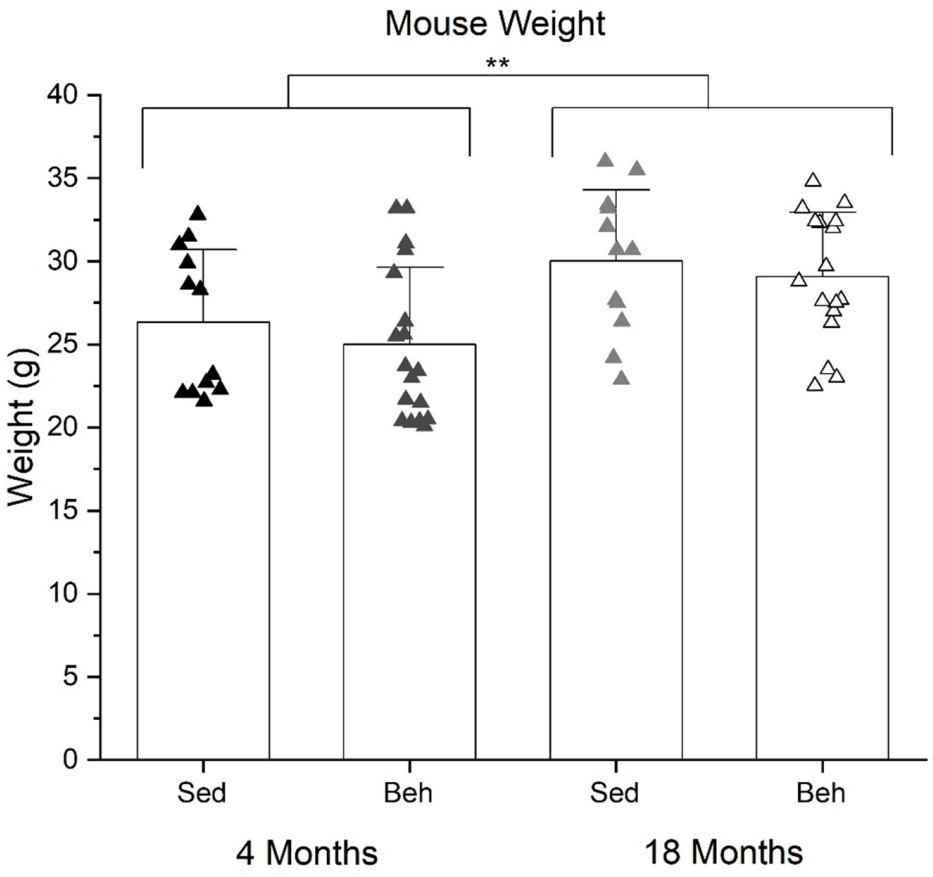
Mouse Weight
**
Weight (g)
40
35
30
25
20
15
10
5
0
Sed
Beh
Sed
Beh
4 Months
18 Months

Figure S6